



University of Bremen

Faculty 4 Production Engineering

Master Space Engineering I

Master Thesis

**Design, Fabrication, and Testing
of a 3D-Printed Model Rocket
with Integrated Telemetry
Systems**

Author: Philippos Georgios Moschidis
Mat. Nr. 6254474

Date: 06.06.2025 TBD

1. Reviewer: Dr.-Ing. Benny Rievers
2. Reviewer: Dr.-Ing. Florian Meyer

Supervisors: Dr. Petros Bithas

Philippos Georgios Moschidis

Master Thesis
moschidis.filip@gmail.com
Matriculation Nr. 6254474

*Design, Fabrication, and Testing of a 3D-Printed Model Rocket
with Integrated Telemetry Systems*

*Entwurf, Herstellung und Test einer 3D-gedruckten
Modellrakete mit integrierten Telemetriesystemen*

Reviewers: Prof. Dr.-Ing. Benny Rievers & Dr. Florian Meyer
Supervisors: Dr. Petros Bithas

University of Bremen
Space Engineering I (SpE I)
Faculty 4 Production Engineering
ZARM, Am Fallturm 2
28359 Bremen

Abstract

The Hermes Rocket Project explores the integration of modern technologies into the domain of model rocketry through the design and fabrication of a 3D-printed rocket that incorporates a telemetry system. The objective of this study is to develop a cost-effective and reusable model rocket capable of achieving an apogee in excess of 200 meters. The rocket is designed to collect flight data while it also utilises a camera to analyse the flight trajectory post-flight. The rocket has been designed to be lightweight and stable, while also ensuring structural integrity, based on PETG material and modular 3D-printed components. The flight computer, which has been custom-built, incorporates a Raspberry Pi Zero 2W micro-controller at its core, as well as three sensors: a GPS, an inertial measurement unit (IMU), and a barometric sensor to monitor altitude, pressure, and motion data. This data will be then analysed for post-flight evaluation. The propulsion of the rocket is provided by Klima D9-5 rocket engines, while the design, simulation and stability of the rocket were ensured through the use of OpenRocket software. The recovery system consists of a ripstop nylon parachute. This research demonstrates how 3D printing and modern sensors can improve the ease of use and performance of model rockets, offering valuable insights for educational and amateur aerospace applications. **More to be added after chapters 8, 9 and 10 are written**

Contents

| | |
|--|-----------|
| 1. Introduction | 1 |
| 1.1. Background and Purpose of the Study | 1 |
| 1.2. Objectives of the Hermes Rocket Project | 2 |
| 1.3. Scope and Limitations | 2 |
| 2. Literature Review | 3 |
| 2.1. Overview of Model Rocketry | 3 |
| 2.2. Advances in 3D Printing for Aerospace Applications | 4 |
| 2.3. Role of Flight Computers and Telemetry in Model Rockets | 5 |
| 3. Rocket Design and Fabrication | 6 |
| 3.1. Conceptual Design of the Hermes Rocket | 6 |
| 3.2. Material Selection | 7 |
| 3.2.1. PLA, PETG, ABS, and Carbon Fiber Nylon Properties . . | 7 |
| 3.2.2. Trade-offs in Strength, Weight, and Durability | 8 |
| 3.3. Hermes Rocket Design | 9 |
| 3.3.1. Body Tube | 9 |
| 3.3.2. Nose Cone | 10 |
| 3.3.3. Fins | 11 |
| 3.4. 3D Printing Process | 13 |
| 3.4.1. Printer characteristics and Constraints | 13 |
| 3.4.2. Assembly of Body Tube, Nose Cone, and Shoulder | 13 |
| 3.5. Joining Methods and Structural Testing | 14 |
| 3.5.1. Epoxy Bonding | 14 |
| 3.5.2. Adapter-Based Screwed Connections | 14 |
| 3.5.3. Adapter-Based Threaded Connections | 15 |
| 4. Flight Computer and Sensor Integration | 17 |
| 4.1. Overview of the Flight Computer System | 17 |
| 4.2. Component Selection and Specifications | 18 |
| 4.2.1. Microcontroller | 18 |
| 4.2.2. Sensor Selection | 18 |
| 4.2.3. Raspberry Pi Camera | 20 |
| 4.2.4. Power Supply | 21 |
| 4.3. Sensor integration on Rocket | 23 |
| 4.3.1. Placement of Microcontroller and Battery | 23 |
| 4.3.2. Placement of Sensors and Camera | 24 |
| 4.3.3. Challenges and Design Considerations | 24 |
| 4.4. Telemetry System | 25 |
| 4.4.1. Live Data Transmission and Communication | 25 |
| 4.4.2. Data Logging, Visualization, and Ground Station Integration | 25 |

| | |
|---|-----------|
| 5. Propulsion System | 28 |
| 5.1. Engine Selection and Performance | 28 |
| 5.2. Thrust Curve Analysis | 28 |
| 5.3. Integration with Rocket Design | 29 |
| 6. Rocket Simulation and Stability Analysis | 30 |
| 6.1. Stability Principles | 30 |
| 6.1.1. Center of Gravity (CG) and Center of Pressure (CP) | 30 |
| 6.1.2. Stability Margin and Caliber | 30 |
| 6.2. Weight Distribution | 32 |
| 6.3. OpenRocket Documentation and Justification of Simulation Differences | 33 |
| 6.3.1. How OpenRocket Works and Its Assumptions | 33 |
| 6.3.2. Core Equations and Calculation Methods | 33 |
| 6.3.3. Simulation Assumptions | 34 |
| 6.3.4. OpenRocket Simulation Features and Output Parameters . | 34 |
| 6.3.5. Possible Reasons for Differences | 35 |
| 6.4. OpenRocket Simulations | 35 |
| 6.4.1. Predicted Flight Path and Apogee | 35 |
| 6.4.2. Flight Sensor Simulation | 36 |
| 7. Recovery System Design | 37 |
| 7.1. Parachute Design for Safe Descent Rate | 37 |
| 7.2. Material Selection, Size, and Deployment Mechanism | 38 |
| 8. Testing and Validation | 40 |
| 8.1. Pre-Flight Electronics Validation | 40 |
| 8.2. Launch and Recovery Testing | 41 |
| 8.3. Battery Endurance Test | 41 |
| 8.4. GPS Field Test | 42 |
| 8.5. Ground Testing of Aerodynamic stability Test | 42 |
| 8.6. Post-Flight Adjustments and Improvements | 42 |
| 9. Results and Discussion | 43 |
| 9.1. Overview of Test Flights | 43 |
| 9.2. Flight Data Analysis | 43 |
| 9.2.1. Flight 1: Data overview | 43 |
| 9.2.2. Flight 2: Data overview | 45 |
| 9.2.3. Flight 3: Data overview | 45 |
| 9.2.4. Flight 4: Data overview | 45 |
| 9.3. Performance Comparison and Trends | 45 |
| 9.4. Material and Structural Evaluation | 45 |
| 9.5. Assessment of Flight Computer and Telemetry System | 45 |

| | |
|---|-----------|
| 10. Conclusion and Future Work | 46 |
| 10.1. Summary of Findings | 46 |
| 10.2. Limitations and Challenges Faced | 46 |
| 10.3. Recommendations for Future Work | 46 |
| 10.4. Potential Applications of the Hermes Rocket | 46 |
| A. CAD and 3D Print Files | ii |
| B. Code Implementation | ii |
| B.1. Raspberry Pi Sensor Reading Code | ii |
| C. Component List and Costs | ii |

List of Figures

| | | |
|-----|--|----|
| 1. | Shady Side Academy Rocketry Club, Pittsburgh PA in January 1965. Rocketry enthusiasts from over a half century ago.[Forum, 2017] | 1 |
| 2. | MAYBE ADD FIGURE OF HERMES? | 2 |
| 3. | Four Forces in Flight [Hall, 2023] | 3 |
| 4. | Relativity Space's third generation 3D-printer in its new headquarters, with CEO Tim Ellis standing by for scale. [Sheetz, 2020] | 4 |
| 5. | ADD FIGURE OF HERMES WITH EVERY PART LABELLED IN FUSION360 | 6 |
| 6. | PLA, PETG, and ABS are the most common materials used with filament 3D Printers [Billington,] | 8 |
| 7. | Body Tube of Hermes on Fusion 360 | 9 |
| 8. | Nose cone and Shoulder of Hermes on Fusion 360 | 11 |
| 9. | Fins of Hermes on Fusion 360 | 12 |
| 10. | Hollow Interior Fin Design | 12 |
| 11. | The Original Prusa MINI+ Printer | 13 |
| 12. | The screwed adapter on Fusion360 and printed | 14 |
| 13. | The threaded adapter on Fusion360 and printed | 15 |
| 14. | Octopus Flight Computer | 17 |
| 15. | Raspberry Pi Zero 2W and SparkFun Qwiic/STEMMA QT HAT [Adafruit,] | 18 |
| 16. | Adafruit TDK InvenSense ICM-20948 [Adafruit,] | 20 |
| 17. | Adafruit Mini GPS PA1010D [Adafruit,] | 20 |
| 18. | Raspberry Pi Camera Module 3 - 12MP 120 Degree Wide Angle Lens [Adafruit,] | 21 |
| 19. | LP903450 3.7V 1600mAh Lithium Polymer Battery with the step up converter | 22 |
| 20. | The tube with the Raspberry Pi and sensors | 23 |
| 21. | Camera and GPS | 24 |
| 22. | Data Visualisation | 27 |
| 23. | Klima D9-5 engines | 28 |
| 24. | Thrust Curve of Klima D9-5 Engine | 29 |
| 25. | Engine Mount on Fusion 360 | 29 |
| 26. | The three stability conditions with their CG-CP | 31 |
| 27. | Weight Distribution | 32 |
| 28. | Flight Path Simulation | 36 |
| 29. | | 36 |
| 30. | Orion Spacecraft Parachute | 37 |
| 31. | The parachute | 38 |
| 32. | The parachute system with dimensions | 39 |
| 33. | Telemetry data from the first flight | 44 |

List of Tables

| | | |
|----|--|----|
| 1. | Comparison of 3D Printing Materials | 7 |
| 2. | Comparison of Barometric Pressure Sensors [Adafruit,] | 19 |
| 3. | Requirement Description and Verification Method | 40 |
| 4. | Flight Conditions and Environment Summary | 43 |
| 5. | Component List and Costs | ii |

List of Abbreviations

| | |
|-------------|---|
| ABS | Acrylonitrile Butadiene Styrene |
| CG | Centre of Gravity |
| CP | Centre of Pressure |
| GPS | Global Positioning System |
| IMU | Inertial Measurement Unit |
| NAR | National Association of Rocketry |
| NASA | National Aeronautics and Space Administration |
| PETG | Polyethylene Terephthalate Glycol |
| PLA | Polylactic Acid |

Acknowledgement

I would like to express my deepest gratitude to several individuals whose support and guidance have been instrumental in the completion of my thesis. Firstly, to PAPALIGHT!

1. Introduction

1.1. Background and Purpose of the Study

The field of model rocketry started in the United States in 1957, it resulted from a synthesis of model aviation, the ancient art of pyrotechnics and modern rocket technology has resulted in the development of a novel and innovative approach to the field of model rocketry. Rocketry has been for a long time been a platform for scientific exploration, offering students and hobbyists the opportunity to gain hands-on experience in propulsion, physics, aerodynamics and engineering. In the past, model rockets were constructed by using basic tools and techniques, which restricted their ability to gather and analysis real-time flight data. But as engineering, compact computing, sensor technologies and engine manufacturing developed it created opportunities for the design of high performance lightweight rockets. Additionally the integration of telemetry, advanced sensors and 3D-printing enables greater control over stability, more precise data collection and improved recovery mechanisms. The objective of the Hermes Rocket Project is to combine these technological opportunities with practical applications, thereby demonstrating how modern innovations can extend the limits of model rocketry.

[Stine and Stine, 2004]



Figure 1: Shady Side Academy Rocketry Club, Pittsburgh PA in January 1965. Rocketry enthusiasts from over a half century ago.[Forum, 2017]

1.2. Objectives of the Hermes Rocket Project

The scope of this thesis is to design, construct and launch a 3D-printed model rocket that is equipped with a custom-build flight computer that collects as well as transmits real-time telemetry data. The aim of this project is to explore the difficulties that come with integration of technologies including the Raspberry Pi, high-precision sensors, wireless communication, camera feed and wireless communication into the field of model rocketry. Additionally a 3D printer will be used to in order for the Hermes Rocket Project to optimise weight, guarantee flight stability and finally make sure that the rocket is recovered safely for reusability. This study will provide helpful information and framework to the evolving field of model rocketry by integrating this modern technology with applications in education and amateur rocketry advancements.



Figure 2: MAYBE ADD FIGURE OF HERMES?

1.3. Scope and Limitations

The main focus of this study is to design, manufacture and test the Hermes Rocket. After the 3D-print of the rocket, the assembly of the flight computer and the setup of the telemetry system was achieved several tests were conducted with the objective of achieving a minimum apogee of 200 meters, and a safe recovery, a number of limitations were encountered during the course of the project. Some of these were the maximum print size of the 3D printer, the availability of the materials used for the rocket and the limited engine power as the project was self funded. Additionally as the testing was held under different conditions than the actual flight, some results may not be applicable to all scenarios. Finally it should be noted that the project is an experimental design and not aimed for commercial production.

2. Literature Review

2.1. Overview of Model Rocketry

Model rocketry emerged in the mid-20th century as both an educational and recreational activity. It represents scaled-down, functional versions of actual rockets and is often constructed from lightweight, non-metallic materials like paper, plastic, or cardboard. This ensures affordability and safety, while factory-made solid-propellant motors guarantee reliability. A recovery system, such as a parachute, enables rockets to return safely to the ground, allowing for multiple uses. Prior to 1958, model rocketry faced safety concerns, leading to restrictions in many regions. The establishment of organizations like the National Association of Rocketry (NAR) introduced standardized safety codes, making model rocketry a safe and popular hobby. Today, it is widely used as an educational tool, promoting STEM concepts in schools, universities, and space camps. [Stine and Stine, 2004]

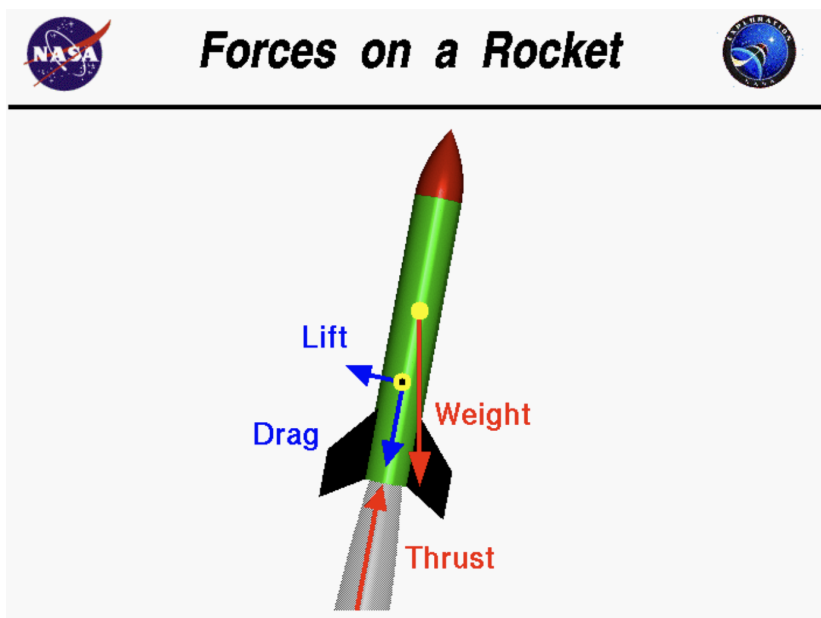


Figure 3: Four Forces in Flight [Hall, 2023]

Similar to aircraft, model rockets experience four primary forces during flight: weight, thrust, lift, and drag as they can also be seen in Figure 3.

- Weight refers to the gravitational force acting on the rocket's combined mass, pulling it toward the Earth.
- Thrust counteracts weight, enabling the rocket to overcome gravity and achieve lift-off.

- Lift stabilizes and controls the rocket's flight direction.
- Drag is the air resistance opposing motion through the atmosphere.

A key factor in stable flight is the relationship between the centre of gravity (CG) and the centre of pressure (CP). For a rocket to maintain stability, the CP (determined by aerodynamic forces) must be positioned below the CG. This configuration ensures that, in the presence of wind or other disturbances, the rocket naturally returns to its intended flight path. [Hall, 2023]

2.2. Advances in 3D Printing for Aerospace Applications

The advent of 3D printing technology has initiated a new era in manufacturing, offering unparalleled opportunities for innovation and efficiency across a multitude of industries. In particular, the aerospace industry stands to benefit from the precision, durability, weight, rigid prototyping, and customization that 3D printing offers. The materials used in additive manufacturing include PLA, PETG, ABS, and composites such as carbon-fibre-infused filaments. These materials are distinguished by their strength, lightweight quality, and ability to produce intricate geometries that are not feasible with traditional manufacturing. Prominent aerospace companies that have adopted 3D printing include SpaceX, NASA, and Relativity Space. [Wawryniuk et al., 2024]



Figure 4: Relativity Space's third generation 3D-printer in its new headquarters, with CEO Tim Ellis standing by for scale. [Sheetz, 2020]

The application of additive manufacturing extends beyond the aerospace industry, as exemplified by its use in the construction of model rockets. In partic-

ular, the costs are significantly reduced in comparison to traditional machining, thereby making advanced designs accessible to hobbyists. This is achieved by utilising 3D printing to create lightweight structures, whereby the wall thickness, internal infill and material density can be controlled.

2.3. Role of Flight Computers and Telemetry in Model Rockets

As previously stated, flight computers have become a crucial component in the field of modern model rocketry, offering enthusiasts the ability to gather real-time data, monitor telemetry, and utilise autonomous control mechanisms. To be more precise, data collection refers to the gathering of information regarding altitude, velocity, orientation, temperature and pressure. This data can be recorded in real time during the flight for subsequent analysis. With regard to the telemetry system, this enables the transmission of live data to a ground station, thereby facilitating insights into the conditions of the flight. This enables the formulation of solutions to any issues that may arise with the rocket, including its position. Furthermore, flight computers can automate parachute deployment, thereby ensuring the safe return of the rocket. This can be achieved through the use of time-based triggers. In bigger scale rockets, the flights computers that are used there are capable of helping with stability of the rocket through the processing of the IMU data and the by correcting manoeuvres. But although flight computers can have many advantages, they also could present challenges. In order for the flight computer to function it needs a power source here the problem could be the managements of this power as a stable supply is crucial for maintaining data integrity and preventing system failure. Additionally, external factor like vibrations, extreme temperatures, and rapid pressure changes can impact the accuracy and reliability of the sensors. [Stine and Stine, 2004]

With reference to modern rocketry, there has been a notable increase in the accessibility of microcontrollers and sensors to the general public. This development has resulted in a significant role for flight computers in the collection of real-time data, the utilisation of telemetry, and the implementation of recovery mechanisms. The core of the flight computer is the microcontroller, which is primarily responsible for processing the data obtained from various sensors. These sensors may include a barometric sensor for measuring altitude, an inertial measurement unit (IMU) for stabilisation and orientation, and a global positioning system (GPS) for tracking. To facilitate live telemetry, wireless communication is essential, and onboard power management is necessary to ensure stable operation during flight.

3. Rocket Design and Fabrication

3.1. Conceptual Design of the Hermes Rocket

The scope of the Hermes Rocket is to design a 3D printed rocket that is capable of being reusable in order to collect data and have a live telemetry. For this to be achieved, the rocket includes a flight computer, a camera and sensors for real-time collection of data. The objective of the mission is to achieve an apogee of over 200 metres, which will enable the flight computer and camera to gather a substantial amount of real-time telemetry and onboard video data for subsequent post-flight analysis.



Figure 5: ADD FIGURE OF HERMES WITH EVERY PART
LABELLED IN FUSION360

The principal structural elements of the rocket are as follows:

- The body tube constitutes the primary structural component of the rocket. This constitutes the primary structural element of the rocket, wherein the flight computer, sensors, power supply and parachute for safe descent and durability will be positioned.
- The nose cone is a crucial component of the rocket, serving several purposes. The nose cone is positioned on the upper portion of the rocket and is designed with an aerodynamic shape to minimise drag.
- The function of the fins is to maintain stability and control during flight. Their design is based on principles of weight distribution and aerodynamics.
- The engine mount is a device which is used to attach the rocket engine to the rocket structure. This is the location where the Klima D9-5 engines are situated, providing the thrust required for the rocket's ascent.

The design philosophy is based on the principles of lightweight modularity. This approach allows for the construction of a rocket that is both lightweight and easily repairable. In case there would be a failure during any of the flights, the rocket could be re manufactured using the 3D printer, as the material is already bought and there is no need for additional design of the parts. The basic

design of the rocket, as well as the flight simulations and stability analysis, were created using OpenRocket. For the design of specific parts of the rocket the CAD application Fusion 360 was used for 3D modelling.

3.2. Material Selection

Selecting the correct material for the manufacturing of the rocket is of great importance as it will impact its design and performance. In more detail the material will have an affect on the structural integrity, the aerodynamic efficiency, the thermal resistance as well as the overall weight. Factors that are essential for achieving a stable flight. In this section, a comparative analysis of the most commonly used 3D printing materials, namely Polylactic Acid (PLA), Polyethylene Terephthalate Glycol (PETG), Acrylonitrile Butadiene Styrene (ABS) and Carbon Fibre Nylon is made, with respect to their strength, weaknesses, sustainability and price for the Hermes rocket. Every individual material has its distinctive advantages and disadvantages, thus it is important to select the optimal material that meets the most performance objectives for the rocket. [Wawryniuk et al., 2024]

3.2.1. PLA, PETG, ABS, and Carbon Fiber Nylon Properties

The table below compares the properties of commonly used 3D printing materials.

| Material | Strengths | Weaknesses |
|--------------------|--|---|
| PLA | - Easy to print - Lightweight - Cost efficient | - Low heat resistance softens $\sim 60^{\circ}\text{C}$. - Brittle |
| PETG | - Tough and flexible - Better heat resistance than PLA softens $\sim 80^{\circ}\text{C}$ - Slightly more expensive than the PLA | - Slightly harder to print than PLA - Slightly heavier than PLA |
| ABS | - Strong, durable and impact resistant - Better heat resistance than PLA softens $\sim 100^{\circ}\text{C}$ - Good machinability | - Dangerous fumes during printing - Tends to warp and crack |
| Carbon Fiber Nylon | - High heat resistance and vibration durability softens $>100^{\circ}\text{C}$ - Flexible and excellent mechanical properties | - Expensive - More difficult to print |

Table 1: Comparison of 3D Printing Materials

3.2.2. Trade-offs in Strength, Weight, and Durability

In order to select an appropriate material for the 3D printer, it is essential to consider the strengths and weaknesses of each material. It is of great importance that the rocket is sufficiently robust to withstand the launch and flight. However, it is also important to consider that the use of materials that are excessively strong but also heavy may have a detrimental impact on engine efficiency and apogee, as lighter materials facilitate enhanced performance. Additionally, it is necessary to consider that as the engines ignite, they generate heat within the rocket, necessitating a material that is both heat-resistant and capable of maintaining its structural integrity under the influence of vibrations.

As can be observed from Table 1, PLA is brittle and therefore unsuitable for applications involving high vibration or stress. In contrast, PETG, ABS and Carbon Fiber Nylon are characterised by high levels of toughness, with the latter exhibiting the greatest resilience. In terms of weight, PLA has the lowest mass, with PETG being a close competitor. ABS and Carbon Fiber Nylon have the highest mass. Ultimately, PLA and ABS are susceptible to cracking, although the latter displays greater resilience to elevated temperatures. Furthermore, PETG exhibits greater heat resistance than PLA, as well as greater durability than the other materials. Finally, Carbon Fiber Nylon displays exceptional durability and can withstand high temperatures. [MarkForged, 2024] [Slump, 2021]

A comparison of the data in the table, together with the information on strength, weight and durability, allows us to conclude that Carbon Fiber Nylon is the optimal choice, with PETG being a viable alternative. However, when considering cost, it becomes evident that Carbon Fiber Nylon is considerably more expensive than PETG. Consequently, the selected material for the Hermes rocket will be PETG.

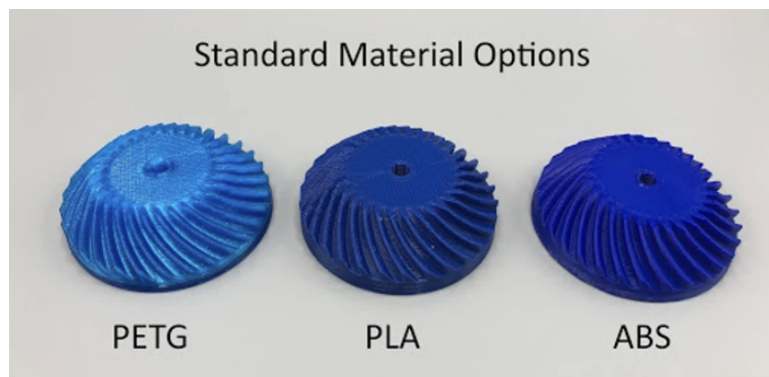


Figure 6: PLA, PETG, and ABS are the most common materials used with filament 3D Printers [Billington,]

3.3. Hermes Rocket Design

This section will address the design of the rocket and the weight of each component. A number of design guidelines and rules of thumb are employed in the field of rocketry. These rules will optimise performance, stability and aerodynamic efficiency. Prior to the design of the Hermes rocket, it is essential to consider a number of key factors in order to develop an effective and efficient design. It is of the utmost importance to consider the internal diameter of the body, as this will determine the location of the flight computer. The largest component of the flight computer has dimensions of $65 \times 30 \text{mm}$, which equates to a diameter of 6.7cm .

3.3.1. Body Tube

With regard to the body tube, a rule of thumb for stability is that the length of the body tube should be approximately $9\text{--}10$ times the maximum diameter of the rocket. Given a diameter of 6.7cm and a total length of 67cm , the outer diameter is 6.7cm and a suitable wall thickness for a robust and flexible body tube is 0.18cm . These dimensions allow us to calculate the weight of the body tube. The material selected for this calculation is PETG, which has a density of $1.15 \frac{\text{g}}{\text{cm}^3}$ [Stine and Stine, 2004]

- First step is to calculate the inner radius:

$$\text{Inner Radius} = \text{Outer Radius} - \text{Wall Thickness} = 3.35 - 0.18 = 3.17\text{cm}$$

- Next step is to calculate the volume:

$$V_{\text{Body Tube}} = \pi \cdot h_{\text{Body Tube}} \cdot (r_{\text{outer}}^2 - r_{\text{inner}}^2) = \pi \cdot 67 \cdot (3.35^2 - 3.17^2) = \pi \cdot 67 \cdot 1.1736 = 247.02\text{cm}^3$$

- Finally for the weight calculation:

$$Weight_{\text{Body Tube}} = Volume \cdot Density = 247.02 \cdot 1.15 = 284.08\text{grams}$$

Therefore, the final mass of the body tube is determined to be 284.08grams .

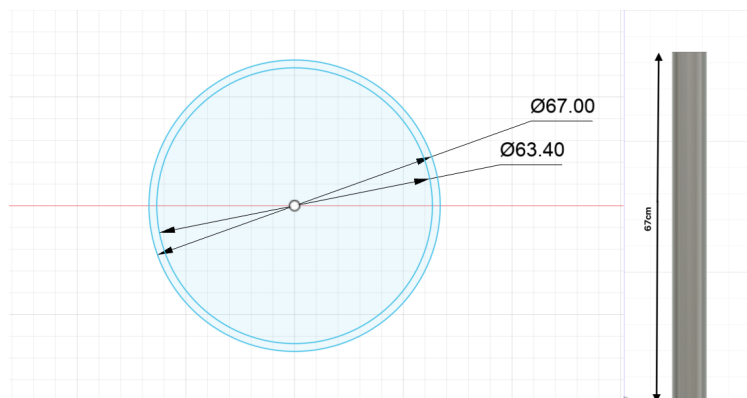


Figure 7: Body Tube of Hermes on Fusion 360

3.3.2. Nose Cone

The shape of the nose cone has an impact on the drag. The most common shapes observed in practice include conical, ogive and parabolic. The aforementioned shapes are typically more aerodynamically efficient than a simple conical shape. Furthermore, the ogive shape is more readily printable than the parabolic, which is why this shape is typically selected. With regard to length, a widely accepted guideline is to maintain a ratio of between three and five times the diameter of the base to the length of the nose cone. This will ensure that the nose cone effectively reduces drag while also maintaining stability. Given that the diameter of the rocket is 6.7cm , the length of the nose cone will be 20cm . In order to calculate the weight, the following steps must be undertaken. [Barrowman and Boyce, 1966]

- First step is to calculate the inner radius:

$$\text{Inner Radius} = \text{Outer Radius} - \text{Wall Thickness} = 3.35 - 0.18 = 3.17\text{cm}$$

- Next step is to calculate the volume:

$$V_{\text{Nose Cone}} = \frac{1}{3} \cdot \pi \cdot h_{\text{Nose Cone}} \cdot (r_{\text{outer}}^2 - r_{\text{inner}}^2) = \frac{1}{3} \cdot \pi \cdot 20 \cdot (3.35^2 - 3.17^2) = \frac{1}{3} \cdot \pi \cdot 20 \cdot 1.1736 = 24.57\text{cm}^3$$

- Finally for the weight calculation:

$$Weight_{\text{Body Tube}} = Volume \cdot Density = 24.57 \cdot 1.15 = 28.26\text{grams}$$

It is also important to consider the shoulder of the nose cone. It is essential that the shoulder is of sufficient length to ensure stability during flight and to maintain the secure attachment of the nose cone to the body tube until the parachute deployment. The length of the shoulder should be sufficient to ensure that, upon ejection of the engines, the parachute is effectively deployed. The length of the shoulder is typically 1 to 1.5 times the diameter of the body tube. This would equate to a length of 5.7cm for the shoulder. In this case, the wall thickness does not have to be the same as that of the body tube or the nose cone, but it can be thinner. In this instance, it will be 0.1cm . In order to calculate the weight of the shoulder, the following steps must be taken: [Stine and Stine, 2004]

- First step is to calculate the inner radius:

$$\text{Inner Radius} = \text{Outer Radius} - \text{Wall Thickness} = 3.35 - 0.1 = 3.25\text{cm}$$

- Next step is to calculate the volume:

$$V_{\text{Shoulder}} = \pi \cdot h_{\text{Shoulder}} \cdot (r_{\text{outer}}^2 - r_{\text{inner}}^2) = \pi \cdot 5.7 \cdot (3.35^2 - 3.25^2) = \pi \cdot 5.7 \cdot 0.66 = 11.81\text{cm}^3$$

- Finally for the weight calculation:

$$Weight_{\text{Shoulder}} = Volume \cdot Density = 14.51 \cdot 1.15 = 13.59\text{grams}$$

The final mass is obtained by adding the weight of the nose cone and the shoulder, resulting in a value of $54.41 + 13.59 = 64.31\text{grams}$. The actual final volume based on the CAD file is 60.18cm^3 meaning that:

Finally for the weight calculation:

$$Weight_{NC\&Shoulder} = Volume \cdot Density = 60.18 \cdot 1.15 = 69.2\text{grams}$$

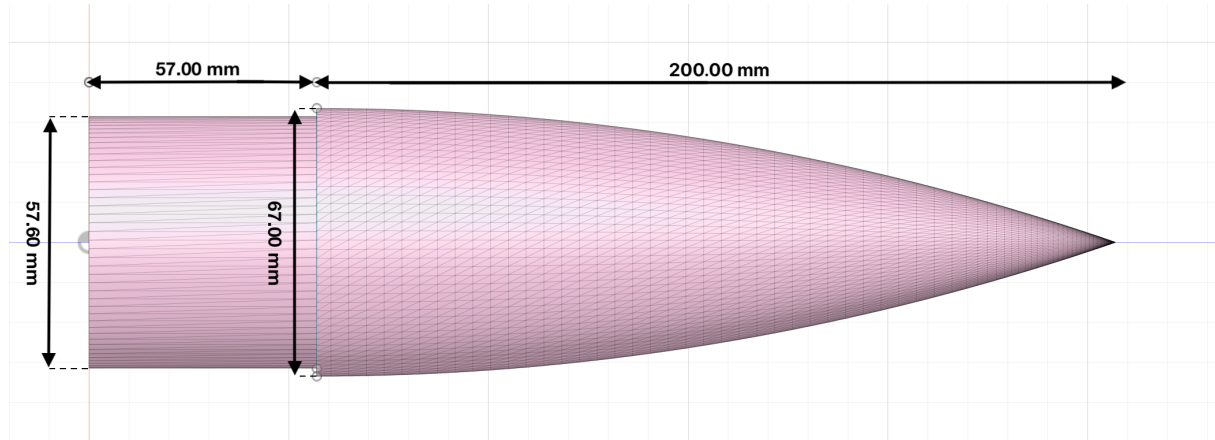


Figure 8: Nose cone and Shoulder of Hermes on Fusion 360

3.3.3. Fins

The fins on a model rocket are of significant importance, as they are integral to the rocket's stability. They ensure that the rocket maintains a straight trajectory and prevents it from exhibiting any lateral movement. Typically, a rocket is equipped with three or four fins, Hermes has four. A common rule of thumb is to make the fin height 0.5 to 1.2 times the rocket diameter. Given that the diameter of the Hermes model rocket is 6.7cm, the height of the fins should be 7cm. The root chord should be between one-and-a-half and one times the rocket's diameter. In this case, the root chord will be 8cm. The tip chord is typically between 50 and 80 percent of the root chord, which in this case will be 6cm. With regard to the sweep length, this should be between 60 and 80 percent of the root chord, here it is 6.7cm. The optimal sweep angle is between 30 and 45 percent of the root chord in this case it is 43.7°. The thickness of the fins should be 0.5cm to ensure sufficient strength while maintaining a low weight. These dimensions are illustrated in Figure 9 below and they will allow us to calculate the weight of the fins. The material selected for this calculation is PETG, which has a density of $1.15 \frac{\text{g}}{\text{cm}^3}$ [Stine and Stine, 2004]

The fins were designed with a hollow interior in order to optimise weight. While a typical single-piece fin is more straightforward to manufacture, it would result in an excess of mass that could have a detrimental impact on the rocket's stability margin and apogee. In order to address this issue, the two-part design consists of one edge wall layer which has a flat base and a wall attach and another flat base by itself, as it can be seen in Figure 10.

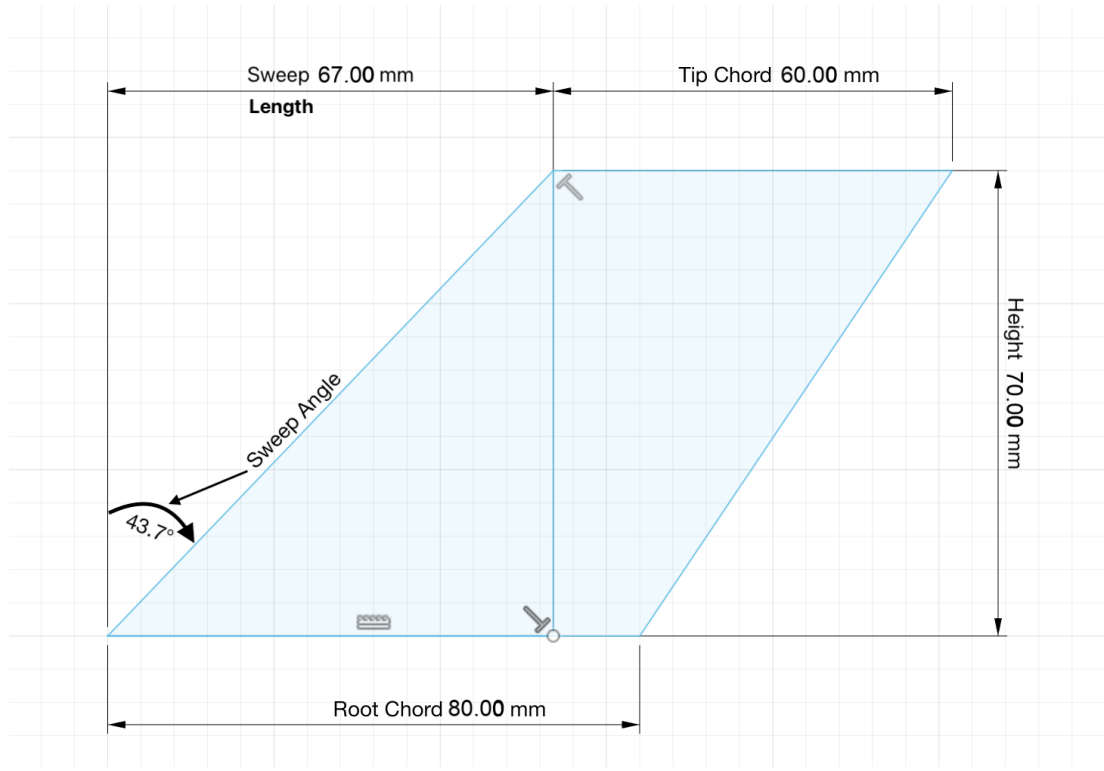


Figure 9: Fins of Hermes on Fusion 360

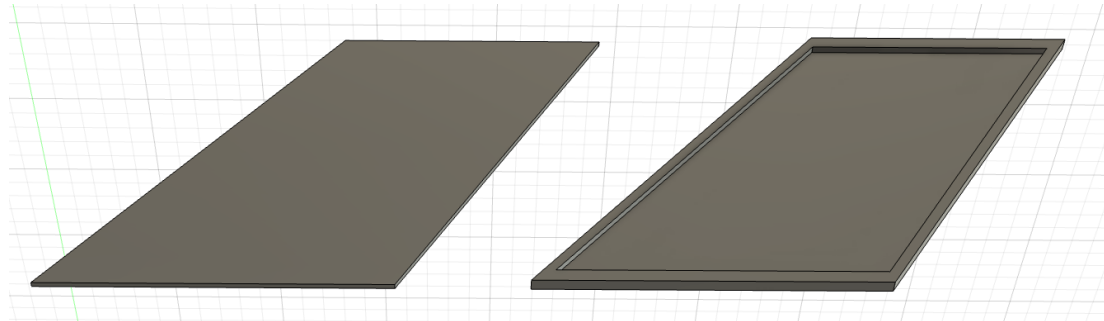


Figure 10: Hollow Interior Fin Design

The hollow design results in a notable reduction in the mass of the fins without any compromise to their strength or aerodynamic properties.

- Weight calculation:

$$Weight_{Fin} = Volume \cdot Density = 16.2 \cdot 1.15 = 18.6\text{grams}$$

- As we have four fins:

$$Weight_{Fins} = Weight_{Fin} \cdot \text{Number of Fins} = 18.6 \cdot 4 = 74.5\text{grams}$$

In comparison, had a solid design been employed, the weight of a single fin would have been 28 grams, resulting in a saving of 10 grams per fin.

3.4. 3D Printing Process

3.4.1. Printer characteristics and Constraints

In regard to the 3D printer, the Prusa MINI+ was utilized, which is equipped with a sensor-less homing mechanism, automated mesh bed calibration, interchangeable nozzles, network connectivity, USB printing, and a comprehensive LCD screen displaying full colour. The layer height of the printer ranges from $0.05mm$ to $0.25mm$, with the nozzle set to $0.04mm$ by default and the ability to accommodate filament diameters of up to $1.75mm$. The printer is compatible with a multitude of materials, including PETG, as previously stated. Additionally, the maximum permissible temperature for the nozzle is $280^{\circ}C$, while the maximum permissible temperature for the bed is $100^{\circ}C$. It is also notable that the print volume is $18 \cdot 18 \cdot 18cm$. However, to enable printing of more complex designs and better results, this has been modified to $17 \cdot 17 \cdot 17cm$. [Printers,]



Figure 11: The Original Prusa MINI+ Printer

3.4.2. Assembly of Body Tube, Nose Cone, and Shoulder

The assembly of the Hermes rocket is a process of aligning and connecting the main components in order to ensure structural integrity and aerodynamic efficiency. The four body tubes are stacked in a vertical configuration. The nose cone is affixed to the uppermost body tube via a precision-engineered shoulder joint. This design feature serves two purposes: firstly, to maintain stability during flight, and secondly, to facilitate the deployment of the recovery system. As the rocket is constructed from multiple components, they must be assembled. In the case of components that are to remain connected on a permanent basis, the use of a durable bonding agent such as epoxy glue is essential to ensure a robust and long-lasting attachment. However, in order to facilitate access to the internal components for maintenance or modifications, the modular assembly simplifies

both the construction process and any future adjustments, thereby ensuring flexibility for testing and optimisation.

3.5. Joining Methods and Structural Testing

3.5.1. Epoxy Bonding

In order to achieve an effective epoxy bond with the PETG material, it is essential to utilise a glue that is specifically formulated for this purpose. The J-B Weld Plastic Bonder was selected as the optimal choice. The adhesive has a rapid setting time and is a two-part glue. The adhesive was employed for the fins, both for affixing the edge wall layer to the flat base layer and for attaching the entire fin to the body tube. Furthermore, the adhesive was employed for the nose, as previously stated, due to its two-part printing configuration.

3.5.2. Adapter-Based Screwed Connections

With regard to the adapter connections, the adapter is composed of two rings that are affixed to the interior of the tube. These rings are then glued at the base of one tube and the top of the other. The interior of the adapter features four holes through which the screw and threaded inserts were positioned. This configuration allows for the straightforward disassembly of the body tube, thereby facilitating access to the flight computer. Figure 12 illustrates the adapter in greater detail.

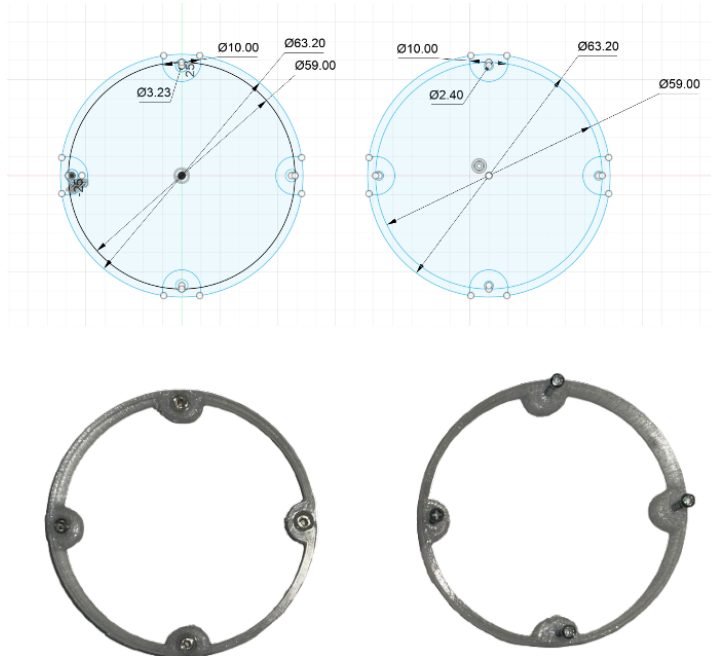


Figure 12: The screwed adapter on Fusion360 and printed

3.5.3. Adapter-Based Threaded Connections

An additional concept for joining methods involved the fabrication of a three-dimensionally printed threaded adapter. In order to create the threaded adapter, two cylindrical components were designed: one male and one female, as illustrated in Figure 13. The female component, situated on the left, has an internal diameter of 59.2 mm, while the male component on the right has an internal diameter of 57.9 mm, thus allowing for a suitable clearance fit. Both components employ an ISO metric thread profile, which exhibits a triangular geometry with a 60° flank angle, thereby ensuring compliance with international standards. The thread size is designated as M58x1.5, where 57.9 mm is the nominal diameter and 1.5 mm is the thread pitch, thereby ensuring a fine and precise fit. With regard to the female component, a 6H tolerance class was selected, representing a standard internal thread fit. In contrast, the male component employs a 6g class, ensuring a medium external tolerance. This combination ensures a reliable, slightly loose fit that accounts for potential inaccuracies inherent to the 3D printing process.

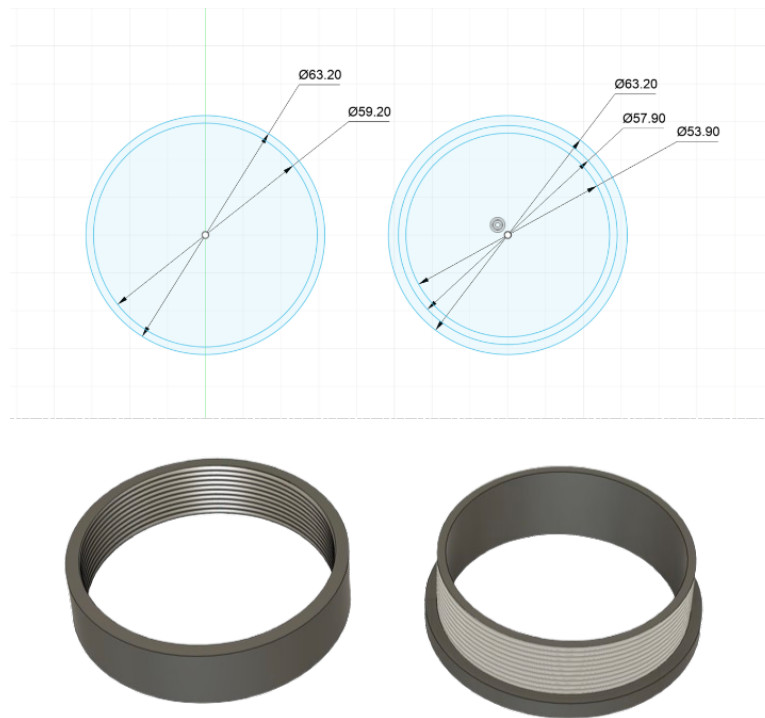


Figure 13: The threaded adapter on Fusion360 and printed

Following a comprehensive evaluation of the three proposed methods, namely epoxy glue, screwed-based adapter and threaded-based adapter, it was determined that the threaded adapter, due to its superior ease and convenience, was the optimal choice. The primary rationale for this determination was the ability

to access all body tubes at any given moment, in contrast to the screwed connection. If modifications were to be made to the body tube in proximity to the engines, the necessity to unscrew every other component would be required.

4. Flight Computer and Sensor Integration

4.1. Overview of the Flight Computer System

The flight computer represents the central component of the rocket, responsible for the aggregation of data collected during the flight. It also serves as the payload of the Hermes Rocket. Its primary function is to monitor and log essential flight information, including altitude, pressure, temperature, and motion data, while simultaneously providing live telemetry to the ground station for real-time analysis. Additionally, it is equipped with a camera for the transmission of video data. This system ensures the accurate collection of data for subsequent post-flight analysis, thereby facilitating the assessment of performance and the validation of the system.

The core components of the flight is the microcontroller, which in this instance is the Raspberry Pi Zero 2W. Additionally, a hat was placed to the Raspberry Pi, which is equipped with Qwiic output, this will facilitate a more straightforward connection with the sensors. Additionally the sensors will be located in various positions across the rocket, thereby saving space and enabling the rocket to be narrower and with an improved weight distribution. The flight computer has a variety of sensors in order to achieve its goals, this includes motion sensors like the IMU, pressure and temperature sensors, a GPS module and a camera module. Details of the specifications, functions and capabilities of the sensors can be found in Section 4.2. Finally the flight computer is powered by a lightweight battery system to ensure stable operation while maintaining the overall weight limits of the Hermes rocket.

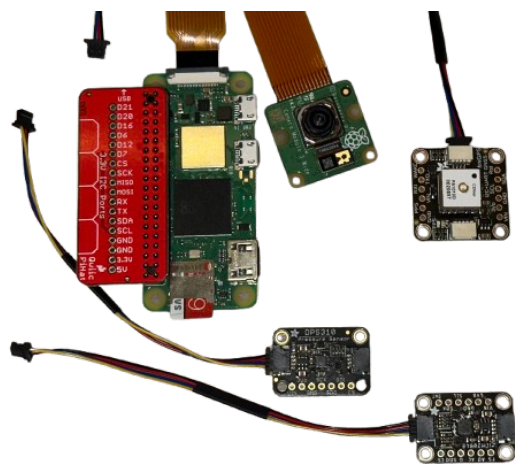


Figure 14: Octopus Flight Computer

4.2. Component Selection and Specifications

4.2.1. Microcontroller

The microcontroller that was selected is the Raspberry Pi Zero 2W due to its compact size, low weight and sufficient computational power to handle real-time data processing and transmission. Alternative options were the Arduino Nano, the Arduino Due, and the STM32F103C8T6 (also referred to as the Blue Pill). But, ultimately these options were unsuitable due to the inability of the Arduino Nano to support additional sensors, the excessive weight of the Arduino Due, and the lack of compatibility with the required camera functionality of the Blue Pill. As for the technical specifications for the Raspberry Pi, it is equipped with a quad-core CPU and 512MB of RAM, which enables it to process multiple sensor inputs and handle real-time telemetry transmission. Finally it has a low power consumption allowing it to operate efficiently on a 7.4W battery setup. [Adafruit,]

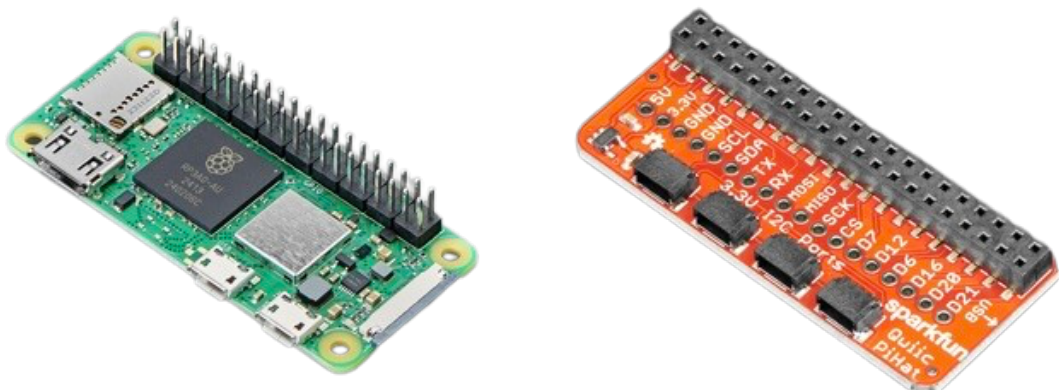


Figure 15: Raspberry Pi Zero 2W and SparkFun Qwiic/STEMMA QT HAT [Adafruit,]

Furthermore, the Raspberry Pi offered the additional option of a Hat, which greatly simplified the connection with the sensors, eliminating the need for soldering. The selected hat is the SparkFun Qwiic/STEMMA QT HAT for Raspberry Pi. The device facilitates the connection of the I2C bus (GND, 3.3V, SDA, and SCL) on the Raspberry Pi to an array of Qwiic connectors on the HAT. The Pi HAT is equipped with four Qwiic connect ports, all on the same I2C bus. Additionally, the device is compatible with any Raspberry Pi or single-board computer with a standard 2x20 GPIO header. [Adafruit,]

4.2.2. Sensor Selection

As for the selection of the pressure sensors, the BMP180, BMP280, BMP388, and the DPS310 were considered. The technical specifications can be seen in Table 2.

By comparing the DPS310 and the BMP388 it can be seen that they are more precise in their pressure measurements and have a considerably broader range than the other sensors. Continuing with the altitude measurements, the DPS310 is the most precise of the sensors, offering a resolution of $0.02m$, which makes it the optimal choice in this context. Furthermore, for the BMP388 and the DPS310 the sampling rate is considerably superior to that of the other sensors, and they are also more efficient during active operation. Also, the DPS310 and BMP388 offer the highest accuracy of $\pm 0.5^{\circ}C$, making them the optimal choice for temperature logging. While the BMP388 is also a strong contender, the DPS310 offers precision, resolution, and low power consumption, making it the most suitable option for flight computers where accuracy and efficiency are of paramount importance. [Adafruit,]

| Feature | BMP180 | BMP280 | BMP388 | DPS310 |
|-----------------------------------|----------------------|--------------------|--------------------|--------------------|
| Pressure Range | 300-1100hPa | 300-1100hPa | 300-1250hPa | 300-1200hPa |
| Pressure Accuracy | $\pm 1.0hPa$ | $\pm 0.12hPa$ | $\pm 0.08hPa$ | $\pm 0.5hPa$ |
| Altitude Resolution | $\sim 0.1 m$ | $\sim 0.1 m$ | $\sim 0.1 m$ | $\sim 0.02 m$ |
| Temperature Range ($^{\circ}C$) | 0 to 65 | -40 to 85 | -40 to 85 | -40 to 85 |
| Temperature Accuracy | $\pm 2.0^{\circ}C$ | $\pm 1.0^{\circ}C$ | $\pm 0.5^{\circ}C$ | $\pm 0.5^{\circ}C$ |
| Sampling Rate | ~ 3 samples/sec | 1 - 25 Hz | 1 - 200 Hz | 1 - 128 Hz |
| Power Consumption | $\sim 12 \mu A$ | $\sim 2.7 \mu A$ | $\sim 3.4 \mu A$ | $\sim 3 \mu A$ |
| Interface | I^2C / SPI | I^2C / SPI | I^2C / SPI | I^2C / SPI |
| Size (mm) | 3.6x3.8x0.93 | 2.0x2.5x0.95 | 2.0x2.0x0.75 | 2.0x2.5x1.0 |

Table 2: Comparison of Barometric Pressure Sensors [Adafruit,]

The range of motion sensors available for selection was less extensive than that of pressure sensors. The principal options were the MPU6050 and the ICM-20948, which may be regarded as a moderately enhanced iteration of the MPU9250. The key differentiating factors between the two are as follows: the MPU6050 is a 6-axis IMU that provides data from accelerometers and gyroscopes, whereas the ICM-20948 is a 9-axis IMU that provides the same data and is also a magnetometer with a $\pm 4900\mu T$ range, enabling full 3D orientation tracking with enhanced precision. The ranges of the accelerometer (*range* : $\pm 2g, \pm 4g, \pm 8g, \pm 16g$) and the gyroscope (*range* : $\pm 250, \pm 500, \pm 1000, \pm 2000^{\circ}/s$) are identical. Moreover, the ICM-20948 exhibits markedly superior power efficiency, consuming only 1.23mA in contrast to the 3.6mA consumed by the MPU6050. The ICM-20948 operates

at a voltage range of 1.71V to 3.6V, whereas the MPU6050 necessitates a voltage range of 3.3V to 5V. Furthermore, both sensors have comparable sampling rates. Finally, the ICM-20948 has a smaller size and supports both I2C and SPI, and can be readily obtained with STEMMA QT/Qwiic connectors. Therefore, the ICM-20948, with its 9-axis capability, magnetometer integration, and low power consumption, is more suitable for high-precision orientation tracking. [Adafruit,]



Figure 16: Adafruit TDK InvenSense ICM-20948 [Adafruit,]

In regard to the GPS selection, given that the microcontroller in use is the Raspberry Pi with Qwiic connectors, the sole viable option is the Adafruit Mini GPS PA1010D. The device is a compact and efficient GNSS module that supports the GPS satellite system and offers a position accuracy of ± 3 meters and a timing accuracy of ± 30 nanoseconds under open-sky conditions. The module operates within a voltage range of 3.0V to 4.2V, with an active power consumption of approximately 20 mA. Furthermore, the device incorporates a built-in ceramic patch antenna, ensuring reliable operation in challenging environments. Furthermore, the device is designed to withstand extreme conditions, with an operating temperature range of -40°C to $+85^{\circ}\text{C}$ and a maximum altitude of 18000 metres, making it well-suited for high-altitude rocket flights. Ultimately, its compact dimensions ($11\text{mm} \cdot 11\text{mm} \cdot 2.2\text{mm}$) and lightweight design (approximately 1 gram) make it an optimal selection for this project. [Adafruit,]

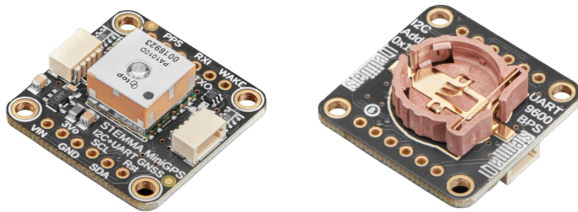


Figure 17: Adafruit Mini GPS PA1010D [Adafruit,]

4.2.3. Raspberry Pi Camera

In regard to the camera selected for this project, the decision to utilise the Raspberry Pi Camera was an appropriate one, given that it is easily connected to the

microcontroller, which has a designated port for this purpose. This choice was made in light of the fact that the microcontroller in use is the Raspberry Pi. Three options were available: the Raspberry Pi camera module 2, the camera module 3, and the camera module 3 with a wide-angle lens. The second generation has an 8-megapixel resolution, in comparison to the 12-megapixel resolution of both the Camera Module 3 options, which also support autofocus and high dynamic range. The field of view represents a further distinguishing feature between the models. The module 2 offers a horizontal field of view of 62.2°, the standard module 3 a 66° field of view, and the wide lens a 120° field of view. The remaining features, including the CSI interface, weight (approximately 3 grams), low power consumption, and dimensions, are largely consistent across the options. With regard to cost, the module 3 is available at a comparable price point. For this project, the camera module 3 (wide lens) is the optimal choice due to its capacity to capture a broader perspective, which aligns well with the requirements of dynamic, high-altitude environments. [Adafruit,]

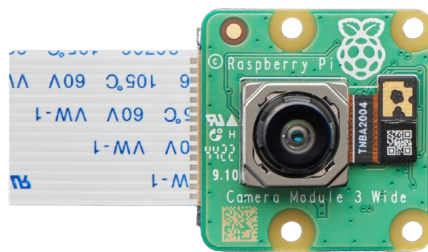


Figure 18: Raspberry Pi Camera Module 3 - 12MP 120 Degree Wide Angle Lens [Adafruit,]

4.2.4. Power Supply

The power supply represents a crucial element of the flight computer system, ensuring the dependable functioning of all electronic components throughout the rocket's flight. The system has been designed to meet the electrical requirements of the Raspberry Pi Zero 2W, sensors and camera module, while also maintaining a lightweight and compact design. The total power requirement of the flight computer system was calculated based on the following components: The Raspberry Pi Zero 2W has a typical consumption of 1.2W at 5V, the DPS310 and ICM-20948 sensors have a combined power consumption of less than 5mA, the GPS module has around 20mA consumption during operation and the Camera Module 3 has an additional load of 200mA during active recording. In order to calculate the power consumption, the following calculations were performed:

- Raspberry Pi Zero 2W:

$$\text{Current}(mA) = \frac{\text{Power}(W)}{\text{Voltage}(V)} = \frac{1.2}{5} = 250mA$$

- Adding up current consumption of all the components:

$$\text{Total Current Draw} = 240(P_i) + 5(\text{Sensors}) + 20(\text{GPS}) + 200(\text{Camera}) = 465mA$$
- Assuming the entire system operates continuously 15 minutes which includes the testing of the Flight computer before launch and the flight, the conversion into hours is:

$$\text{Flight Duration (hours)} = \frac{15}{60} = 0.25\text{hours}$$
- The total energy consumed during this time is:

$$\text{Energy Required (mAh)} = \text{Current Draw (mA)} \cdot \text{Flight Duration (hours)}$$

$$\text{Energy Required (mAh)} = 465mA \cdot 0.25 = 116.25mAh$$

In order to satisfy the specified requirements, it is necessary to utilise a battery with a voltage exceeding 5V and a total capacity of 1000mAh, in order to accommodate safety margins. Consequently, the selected battery was the Cellevia Battery LP903450, which is a 3.7V, 1600mAh Lithium Polymer Battery. Additionally, a step-up converter was employed in order to upgrade the voltage output.



Figure 19: LP903450 3.7V 1600mAh Lithium Polymer Battery with the step up converter

4.3. Sensor integration on Rocket

The positioning of sensors is of paramount importance for ensuring the stability of a rocket, given that the weight distribution is not uniform and one side of the rocket may be more heavily loaded than the other. This disparity in weight distribution can result in a tilt towards the more heavily loaded side during flight. The flexibility in sensor placement afforded by the cables extending from the flight computer allows for sensors to be positioned in a range of locations. To this end, a tube has been printed for the ejection charge to go through it, for placing the Raspberry, battery, IMU and pressure sensor. Also mounts have been developed to facilitate the positioning of the camera and GPS, thereby ensuring balance and preventing the rocket from tilting during flight. At the top and bottom of the tube I design another part that keeps the tube centred and the bottom I also printed two half circles in order to protect the flight computer from the ejection charge.

4.3.1. Placement of Microcontroller and Battery

The flight computer is composed of several components, the heaviest of which are the battery and the Raspberry with the hat, which weigh 32 and 26 grams respectively. These components are positioned at the centre of the rocket. This is also evident in Figure 20. The Raspberry Pi and the battery's integration within the rocket is facilitated by the utilisation of tape, a method that ensures its precise placement in the confined space of the rocket.

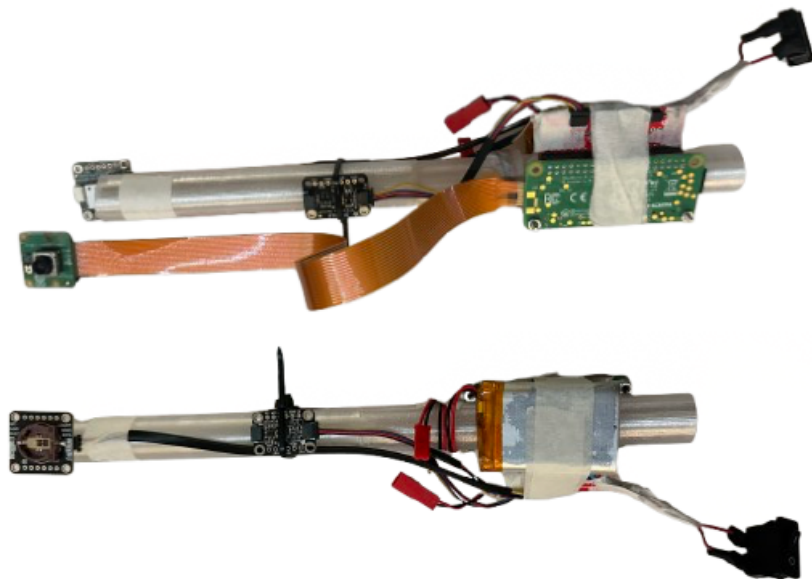


Figure 20: The tube with the Raspberry Pi and sensors

4.3.2. Placement of Sensors and Camera

The sensors of the flight computer are located at a point 10 centimetres above the battery and the Raspberry. The IMU accelerometer and gyroscope, as well as the DPS pressure sensors, are positioned at this location. Both sensors have an exact weight of 1 gram and in order to keep them in this position I used tie up. The final sensor is the GPS, which has a weight of 5 grams, and the Raspberry Pi Camera, which also has a weight of 5 grams. These modules have been placed at a height of 6 centimetres above the IMU and DPS sensors. As the camera has to be mounted on the body tube in order to have a view of outside of the rocket, I couldn't place them on the tube. Each corner of the modules is equipped with four holes, enabling them to be positioned on the holes of the body, together with a screw and a nut for safety. Furthermore, a hole was made in the body tube of the rocket to accommodate the camera lens, enabling the external environment to be filmed.

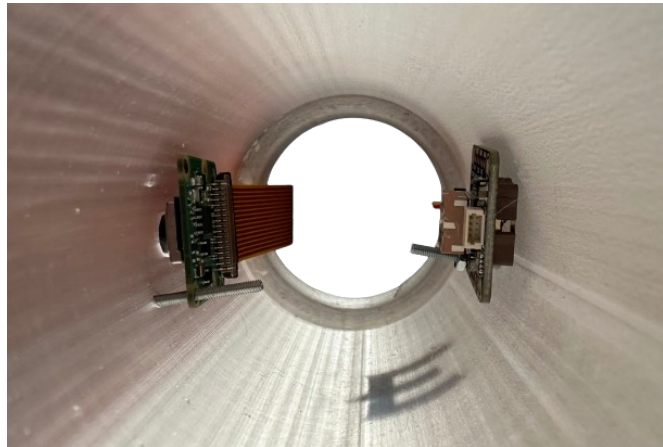


Figure 21: Camera and GPS

4.3.3. Challenges and Design Considerations

The optimal method for mounting the rocket's sensors presented a formidable challenge, primarily due to the compact nature of the sensors and the necessity for lightweight mounts. Additionally, the requirement for unobstructed airflow through the body tube to facilitate the ejection charge's deployment of the parachute was a crucial factor. Initially, the concept of employing oversized mounts that would permit the sensors to slide along the side of the mount was considered. However, these mounts proved to be excessively heavy, impeding their ease of placement on the rocket. The utilisation of silicon foam, a material renowned for its lightness, was contemplated. However, this approach was subsequently abandoned due to its encroachment upon the available space within the rocket's body tube. Subsequently, the concept involved the employment of

small holes in the corners of the sensors, initially pursued through the utilisation of a 3D printer. However, these mounts, being too small, proved to be prone to breaking. Ultimately, the decision was made to employ screws, ensuring precise thickness, to achieve the desired outcome. In order to mount the battery, a mounting apparatus was first designed. However, due to the irregular shape and weight of the battery, it was challenging to position it within the body tube. Consequently, the tube was printed which could then easily mount almost every sensor..

4.4. Telemetry System

The telemetry system is an important part of the Hermes rocket, facilitating real-time monitoring and post-flight analysis of critical flight data. There will be the possibility to transmit live data from onboard sensors to a ground station for the first few meters of the launch, before the Raspberry pi will disconnect from the Wi-Fi. The telemetry system is essential as it provides insight into the rocket's performance during the launch, flight, and recovery phases. This is of great importance to the project, as after the launch potential issues can be analysed and then changed before the next flight.

4.4.1. Live Data Transmission and Communication

In order to facilitate the transmission of sensor data to the ground station, an intermediate component is required. This component is the Raspberry Pi, which possesses the capability to transmit data via Wi-Fi or Bluetooth, in our case the Wi-Fi option was used. The Raspberry Pi's integrated code for data collection from the sensors also incorporates the command to transmit the data to the ground station, which has a dedicated code for this purpose, provided both devices are connected to the same Wi-Fi network. The functionality is further enhanced by the use of a mobile hotspot, as the launch site does not have Wi-Fi. After the Rocket, essentially the Raspberry pi is out of reach from the mobile hotspot, the script will continue to run, meaning it will still store the data to the micro SD that is placed in the Raspberry.

4.4.2. Data Logging, Visualization, and Ground Station Integration

The ground station, in this case, a MacBook, receives real-time data transmitted via Wi-Fi from the Raspberry Pi flight computer using the UDP protocol. This integration enables the live monitoring of flight parameters such as altitude, temperature, velocity, acceleration, vertical speed, orientation(pitch, roll yaw), rotation rate and finally rocket drift, providing immediate feedback to ensure mission success. Furthermore, the ground station processes and visualizes this data using custom Python scripts and libraries like Matplotlib, offering intuitive

plots that facilitate real-time decision-making and post-flight analysis.

As illustrated in Figure 22, the telemetry comprises a total of eight plots. The temperature plot display the onboard ambient temperature measured degrees Celsius and recorded by a the DPS310 pressure sensor. Next to it is the altitude in both barometric and GPS. It compares the altitude estimated from the barometric sensor again measured in metres and calculated based on pressure while on the same plot we can also determine the altitude from the GPS sensor. The last plot on the top row is the velocity plot, which shows the resultant velocity magnitude calculated from the accelerometer using vector magnitude. On the second row we can see the acceleration magnitude plot, which tracks the intensity of acceleration the rocket is experiencing, which is also derived from the IMU's accelerometer. Next to this is the vertical speed plots which is computed as rate of change of barometric altitude between samples, giving insight into ascent and descent dynamics. Finally on the second row is the orientation plots, which illustrated the angular orientation of the rocket over time, meaning pitch, roll and yaw, this is also derived from the IMU. On the last row is the rotation rate plot which quantifies the overall angular velocity measured specifically from the gyroscope. Finally the rocket drift plots shows the lateral displacement from the GPS.

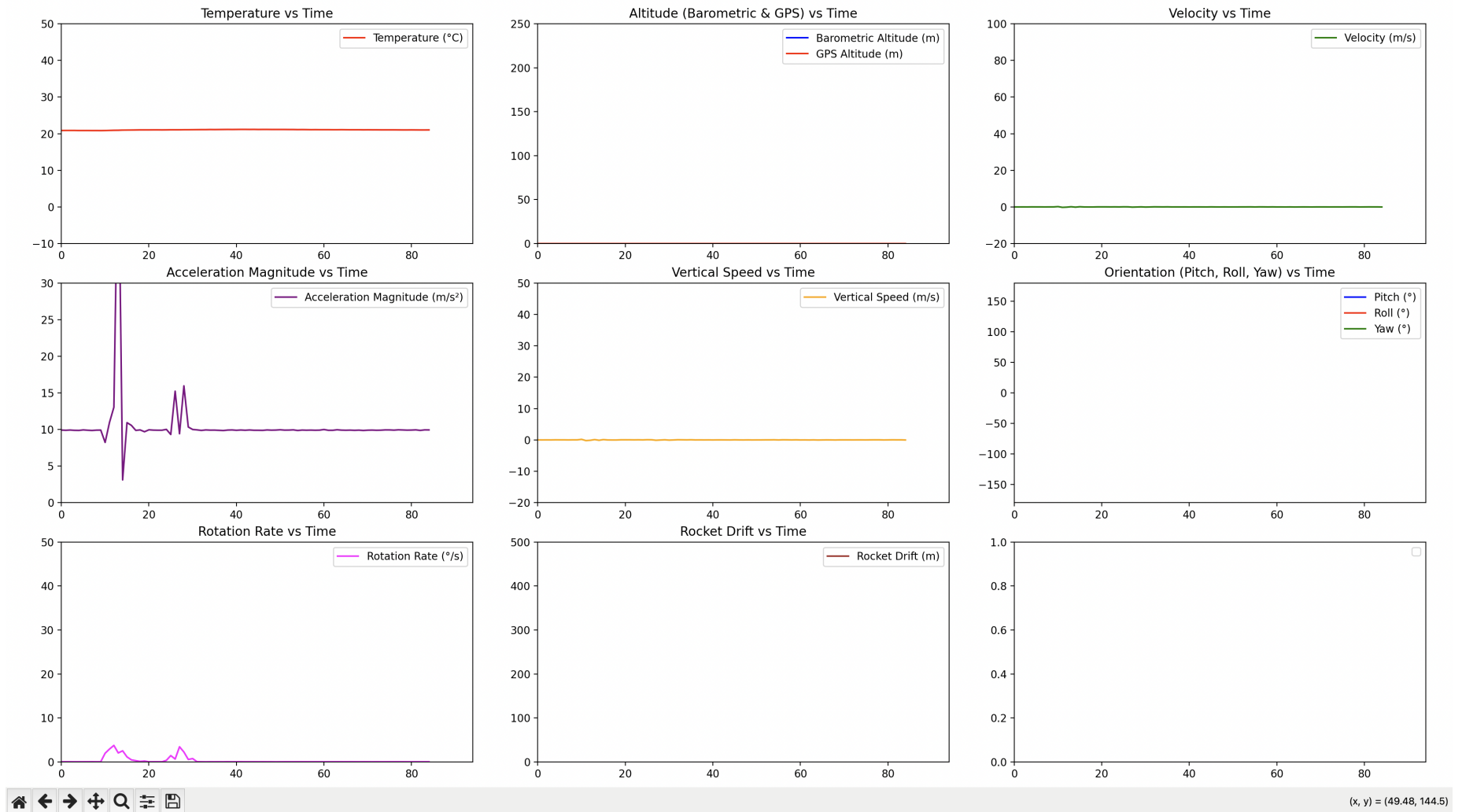


Figure 22: Data Visualisation

5. Propulsion System

5.1. Engine Selection and Performance

The selection of the engines had to be compatible with the rocket's weight, stability margin, target apogee, ejection delay, cost and availability on the market, as well as on the OpenRocket simulator that was used. Given the substantial rocket weight, there was a requirement for powerful engines. Consequently, as a result of the aforementioned considerations, the engines would have to be multiple Klima D-class engines or TSP E-class engines, as the majority of the others are not readily available in Europe. Following a cost-benefit analysis, the Klima D9-5 solid rocket engine was selected. This engine has a total impulse of 20Ns, an average thrust of 9N, a maximum thrust of 25N, a burning period of 2.1s, and a specific ejection delay of 5s, which ensures the recovery system deploys at apogee. The engine's dimensions are 70mm in length and 18mm in diameter, with a total weight of 27g, of which 16g is black powder propellant. It is noteworthy that a single engine would not suffice for the Hermes rocket to surmount Earth's gravitational pull and attain the desired apogee exceeding 200 metres. Consequently, the utilisation of three engines would be the optimal configuration. [thrustcurve.org,]



Figure 23: Klima D9-5 engines

5.2. Thrust Curve Analysis

The thrust curve of the Klima D9-5 engine is a pivotal factor in determining the rocket's flight profile. As illustrated in figure 24, the engine's peak thrust of 20N is attained immediately following the initiation of the ignition process. This results in a rapid acceleration, enabling the rocket to overcome the forces of gravity and drag. Over the 2.1-second burn duration, the thrust gradually decreases, stabilising at an average of 9.2N. This smooth thrust profile is conducive to minimising stress on the rocket's structure while maintaining stability. The total impulse of 20N guarantees that the rocket attains its target apogee under nominal conditions. The thrust curve analysis also ensures that the engine

provides sufficient force to maintain a thrust-to-weight ratio greater than 5:1, a critical parameter for safe and stable flight. [thrustcurve.org,]

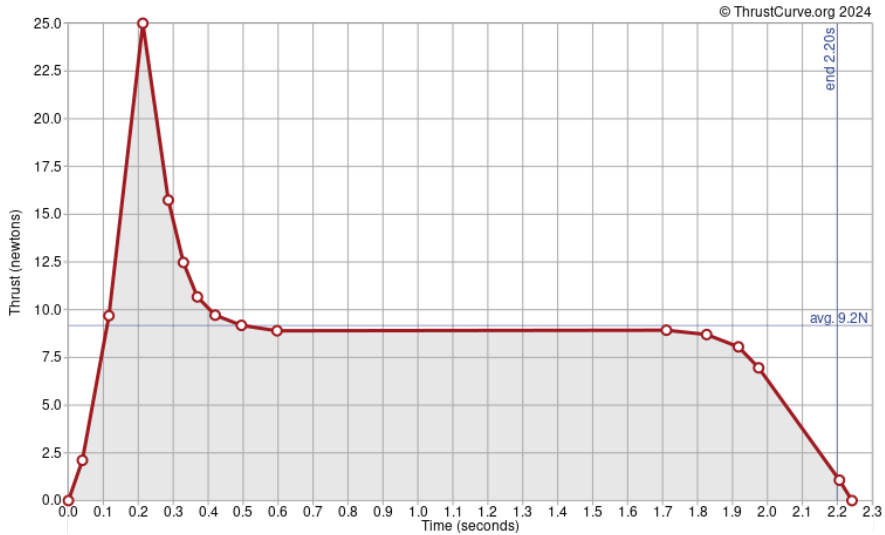


Figure 24: Thrust Curve of Klima D9-5 Engine

5.3. Integration with Rocket Design

The D9-5 engines are mounted in a custom-design engine mount that can be seen in Figure 25. The mount has been designed in a way that fits precisely within the body tube where it was then stabilised with the epoxy glue. This, guarantees the alignment of the thrust vector during the launch phase with the rocket's centre of gravity thereby maintaining stability. In more detail, two engine mounts have been positioned at one and five centimetres from the bottom of the tube. The dimensions of the 3-ring cluster design have an outer diameter of 63.4mm and a thickness of 5mm.

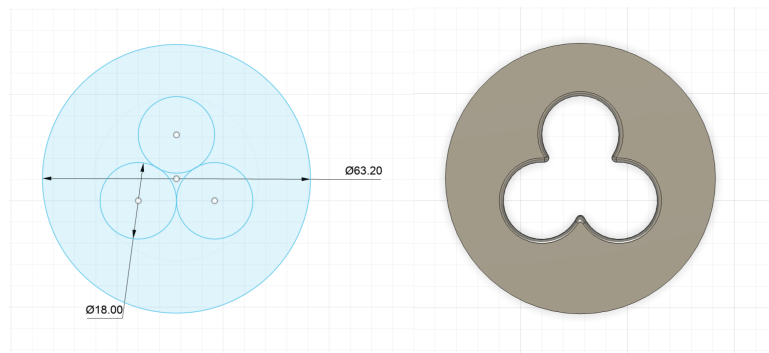


Figure 25: Engine Mount on Fusion 360

6. Rocket Simulation and Stability Analysis

6.1. Stability Principles

Stability is an important part in model rockets, it makes sure that the rocket maintains a predictable and controlled flight trajectory while ascending and descending. Having a stable rocket means that it will not deviate from its planned trajectory due to aerodynamic forces, but instead helps it to achieve this trajectory with precision. The three main objectives of the stability analysis are to optimise the rocket's flight trajectory, to keep it safe and finally to verify that the design parameters are aligned with the aerodynamic criteria. This is achieved by balancing the rocket's Centre of Gravity (CG) and Centre of Pressure (CP) to ensure an adequate stability margin, which is commonly expressed in terms of the rocket's body diameter (Cal). The optimal range for most model rocket is between 1-2 Cal, as it ensures stability but also maintaining manoeuvrability under variable flight conditions. Stability analysis is instrumental in refining design parameters, such as fin size and placement, or internal component distribution, thereby ensuring the rocket's capacity to withstand real-world disturbances, including wind and uneven thrust. The incorporation of these principles into the design process enables engineers to enhance performance, mitigate risks, and ensure the success of mission outcomes. [OpenRocket,]

6.1.1. Center of Gravity (CG) and Center of Pressure (CP)

Rocket stability is governed by the relative positions of the CG and CP. When a free body in space rotates, it spins around an imaginary point where all its mass appears to be concentrated, this is the balance point, or else called the centre of gravity. On the other hand the point where all the aerodynamic forces act is called the centre of pressure.

6.1.2. Stability Margin and Caliber

Having established the definitions of the CG and CP, the subsequent section will address the consequences of these points on the stability of a model rocket. It should be noted that three distinct stability conditions can be identified, as illustrated in Figure 26.

1. Positive stability: In this condition, the model rocket's CG is positioned ahead of the CP. The design of the model rocket is characterised by the presence of large fins set far back on the body tube. This configuration results in the rocket flying straight and weathercocking into the wind at launch.
2. Neutral stability: In this case, the CP and CG are at the same position on the model rocket. This may occur if the rocket has a lightweight nose or

fins that are too small, or both. In the absence of stabilising and restoring forces in the model rocket, this may result in unpredictable paths.

3. Negative stability: In this condition, the CG is behind the CP. In this scenario, the aerodynamic forces on the fins tend to cause the model to fly tail-first, which is not possible under power. As the nose has any pitch or yaw movement, a force exists to keep it swinging, resulting in the model pinwheeling end over end and eventually descending to the ground. [Stine and Stine, 2004]

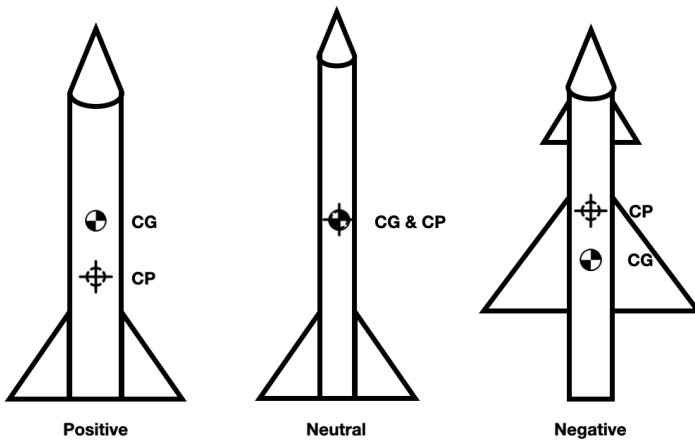


Figure 26: The three stability conditions with their CG-CP

It is imperative that the model rocket has the CG ahead of the CP. In addition, a stability margin, denoted as the caliber, must be considered. This represents the distance between the CG and the CP, expressed in terms of the rocket's body diameter.

- The definition of the caliber is derived from the following equation:

$$Cal = \frac{\text{Distance between CG and CP}}{\text{Body Tube diameter}}$$

There are four interpretation of Cal values:

- 0 cal: The CG and CP are aligned, thereby rendering the rocket highly unstable. This condition has previously been described as neutral stability.
- <1 cal: The rocket is marginally stable and may not be able to fly in a straight path, particularly when subjected to wind disturbances.
- 1-2 cal: The rocket exhibits ideal stability, which is the optimal range for most model rockets. This condition ensures that the rocket flies straight while maintaining sufficient manoeuvrability.

- >2 cal: The rocket may exhibit excessive stability, thereby impeding the process of adjustment and potentially resulting in a deviation from the intended trajectory in the presence of strong winds. [OpenRocket,]

The location of the CG and CP of the Hermes rocket can be determined by observing the OpenRocket application. Specifically, from the tip of the rocket, the CG is situated at *56.7cm* and the CP is at *70.3cm*. This indicates that the Cal value is 2.03, suggesting that the rocket maintains ideal stability and would only deviate from its trajectory in the presence of strong winds.

6.2. Weight Distribution

It is vital to ensure optimal weight distribution within a rocket, as previously discussed, in order to maintain stability and ensure the rocket follows the intended flight path without deviating excessively to either side due to imbalanced weight distribution. In order to achieve this, it is essential that the sensors and all other mass components within the rocket are placed in equal positions. This has been achieved based on the weight of each sensor and then by placing them opposite each other so they can cancel out. To illustrate this approach, the IMU and the DPS310, both of which weigh 1 gram. A similar principle applies to the Camera and GPS, which each weigh *5grams*. The battery and the Raspberry, on the other hand, have weights of *25grams* and *20grams*, respectively. However, the Raspberry also contains the step-up converter and the rocker switcher, which powers the flight computer. These components cancel out the weight difference. The engines are another component that is very heavy, with a total mass of 81 grams, but with the help of the engine mounts, they are positioned centrally. The adapters that connect the body tubes together are in total three, but they are placed in equal distances. Finally, the parachute, which is of equal width to the body tube, is located in close proximity to the first adapter, thus ensuring a centralised positioning of the system.

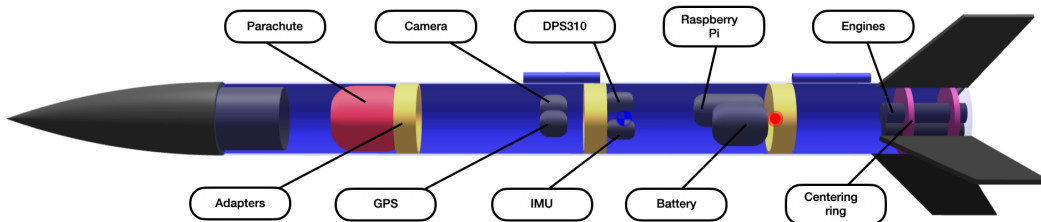


Figure 27: Weight Distribution

6.3. OpenRocket Documentation and Justification of Simulation Differences

6.3.1. How OpenRocket Works and Its Assumptions

The OpenRocket software was utilised for the purpose of simulating the flight of the rockets. OpenRocket is an open-source software that can be used for model rocket simulators. It facilitates the design and simulations of the rockets prior to construction and launch. The utilisation of simulations enables the prediction of key parameters, optimisation of rocket design, and assessment of conditions such as weight distribution, engine clusters, and parachute deployment, with the objective of determining their impact on the overall flight plan. These simulations are founded on established aerodynamic theories and numerical methods to predict the rocket's flight characteristics.

6.3.2. Core Equations and Calculation Methods

As outlined in the master's thesis Development of an Open Source Model Rocket Simulation Software by Sampo Niskanen, the three core equations for OpenRocket can be seen below. [Niskanen, 2009]

1. Stability Calculations:

The initial step in this process is to consider the core equations and calculation methods that are utilised by OpenRocket. For instance, the stability of a rocket is determined by the Barrowman equations. These equations calculate the centre of pressure based on the geometry and configuration of the rocket components. The Barrowman equation is presented below:

- $X_{CP} = \frac{\sum X_i C_{Na,i}}{\sum C_{Na,i}}$

- Where:

X_i is the position of the component's centre of pressure.

$C_{Na,i}$ is the normal force coefficient derivative for the component.

2. Drag Force Estimation:

In the context of drag force estimation, OpenRocket employs a methodology that integrates the following components to estimate drag. Moreover, it is important to acknowledge that, in the context of supersonic flight, the estimation of drag coefficients is typically facilitated through the utilisation of empirical formulas derived from experimental data. However, given the unique characteristics of this particular rocket, a more comprehensive analysis is deemed unnecessary.

- $C_D = C_{D_{body}} + C_{D_{fin}} + C_{D_{base}} + C_{D_{parastic}}$

- Where:

$C_{D_{body}}$ is the drag from the body tube.

$C_{D_{fins}}$ is the drag from the fins.

$C_{D_{base}}$ is the drag from the base due to low-pressure zones.

$C_{D_{body}}$ is the drag from the launch lugs or other small protrusions.

3. Motion Simulation:

In relation to the motion simulation, the rocket flight is simulated by employing the 4th-order Runge-Kutta method to solve the equations of motion. The core equation is as follows:

- $$\frac{d^2x}{dt^2} = \frac{F_{thrust} - F_{drag} - F_{gravity}}{m}$$

- Where:

F_{thrust} is the thrust force from the engine.

F_{drag} is the air resistance or drag force.

$F_{gravity}$ is the gravitational force.

m is the rocket mass, which decreases over time as the fuel burns.

6.3.3. Simulation Assumptions

The core equations and calculation methods alone are insufficient to yield the final result, and consequently, OpenRocket also bases its simulations on a combination of aerodynamic theories and numerical methods, incorporating several assumptions to simplify and optimise the simulation process. Firstly, the rocket is assumed to be axially symmetric. This assumption simplifies the calculations by presuming that the aerodynamic forces are uniformly dispersed along the rocket's axis. This is a common assumption in the majority of traditional rocket designs, where the fins and body components exhibit symmetry. In the context of ideal motor performance, the motor thrust is modelled based on thrust curves provided by the manufacturer. These curves represent optimal conditions and do not consider environmental variations, such as temperature. Consequently, minor discrepancies may emerge in the motor performance predictions. Additionally, OpenRocket simplifies the complex behaviour in the transonic and supersonic regimes by using predefined drag coefficients, thus facilitating high-speed aerodynamics. Unless modified by the user to reflect actual launch conditions, the simulations assume standard atmospheric conditions. Another assumption that, unless explicitly defined, is the wind conditions and turbulence, which are not factored into the simulation. However, these can be changed if the relevant data are available. [Niskanen, 2009]

6.3.4. OpenRocket Simulation Features and Output Parameters

In order to achieve the most accurate simulations on OpenRocket, it is possible to input parameters such as launch conditions, aerodynamic properties, and propulsion data. Following this, the user has the option to generate various plots, including the final trajectory, acceleration and forced acting on the rocket, drag

coefficient vs Mach number, parachute deployment sequence and descent rate, and stability metrics such as CG and CP over time. It has been demonstrated that OpenRocket predictions, when substantiated by experimental validation, exhibit an accuracy of 10-15 percent relative to real flight data. Variations in performance are attributed to wind effects, surface irregularities, and discrepancies in motor performance.

6.3.5. Possible Reasons for Differences

While OpenRocket provides a strong first-order approximation, discrepancies between simulated and real flight data may emerge due to the following factors:

1. Aerodynamic Variations: Small surface imperfections and 3D-printed textures may affect drag coefficient.
2. Wind Disturbances: Actual wind conditions could vary from those modeled in OpenRocket.
3. Structural Flexibility: The rocket body is possible to experience flexing, affecting stability and moment of inertia.
4. Sensor Noise and Calibration: IMU readings from the accelerometer, gyroscope, and magnetometer can introduce errors due to sensor drift or misalignment.
5. Motor Thrust Variability: Manufacturer thrust curves assume ideal conditions, whereas real motors may have burn inconsistencies.

6.4. OpenRocket Simulations

6.4.1. Predicted Flight Path and Apogee

In this section, the focus is on the modelling of the rocket trajectory during its flight. OpenRocket, is capable of simulating the rocket's ascent, apogee, and descent based on the provided parameters. These parameters include engine thrust, rocket weight, and aerodynamics. The predictions made by the software are crucial in determining the rocket's performance and whether it will meet the targeted altitude expectations. The flight path simulation provides information regarding the projected maximum altitude, the time to reach apogee, and the anticipated descent trajectory following complete engine burnout. [OpenRocket,]

As demonstrated in Figure 29, the predicted apogee is 233 metres, which is attained at approximately 7 to 8 seconds. The simulation also provides insights into the motor burnout, the ejection charge, and the deployment of the recovery device. The former occurs approximately two seconds after the initiation of the process, while the latter two occur at approximately seven seconds. This is due

to the ejection delay of five seconds following the engine burnout. Subsequent to the apogee being reached, the rocket will make contact with the ground at approximately 30 seconds, having traversed the air for more than 20 seconds. It should be noted, however, that these times are subject to variation depending on prevailing weather conditions and wind gusts.

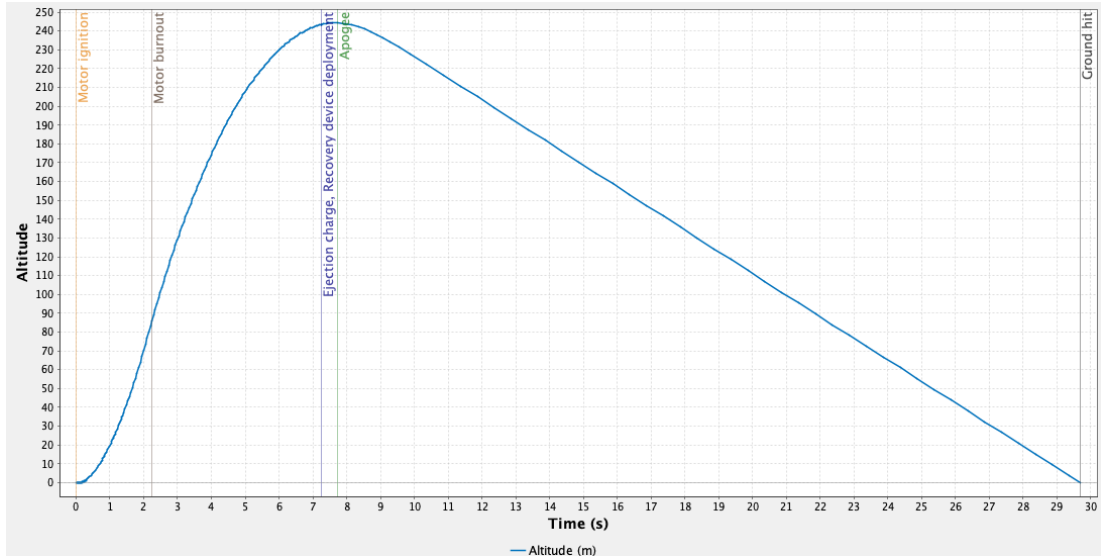


Figure 28: Flight Path Simulation

6.4.2. Flight Sensor Simulation

In the following sections, the focus will be directed towards an examination of the other sensors and the ensuing output data that will be displayed in the telemetry system, with particular reference to the IMU. Specifically, the simulation depicted in Figure 30 illustrates velocity, vertical speed, acceleration magnitude, orientation for pitch, roll and yaw, rotation rate and finally rocket drift.

Figure 29

7. Recovery System Design

The recovery of the rocket in an intact state is of paramount importance in this project, as the rocket is required to be able to fly multiple times and it would also prevent any damage to the flight computer. In this particular project, the parachute recovery system has been selected. This recovery was first used in model rockets by Orville H. Carlisle in 1954, and since then there has been a great deal of research into parachutes, with these systems still being used in many cases today. The parachute is affixed to the rocket's nose cone, and in conjunction with a shock cord, it constitutes a highly reliable recovery system. [Stine and Stine, 2004]



Figure 30: Orion Spacecraft Parachute

7.1. Parachute Design for Safe Descent Rate

Parachutes are available in a variety of shapes, including circular, square, hexagonal, and octagonal designs. The prevalence of circular parachutes is low, as the fabrication process for hexagonal and octagonal parachutes is more straightforward. The parachute's design incorporates a targeted descent rate of $4 - 6 \text{ m/s}$ to ensure a safe and controlled descent while also keeping an easy design using a semi-spherical octagonal. This rate is calculated to minimise the risk of damage to the rocket during landing while ensuring a timely recovery. The diameter of the parachute was calculated using the drag equation, with a resultant measurement of 77 cm. [Stine and Stine, 2004]

- Drag equation:
$$D = W = 0.5\rho V^2 C_d A$$

Where W is the rocket's weight, ρ is the air density, which at sea level is typically 1.225kg/m^3 , V is the desired descent velocity, C_d is the drag coefficient, which for a hemispherical parachute is approximately 1.5, and finally, A is the parachute's area. In greater detail, the parachute area is calculated as follows: $A = \pi(d/2)^2$. In addition, a spill hole with a diameter of 7.5 cm was incorporated into the design to reduce oscillations and enhance stability, whilst also preventing the rocket from spinning. [Apogee Components, 2023]

7.2. Material Selection, Size, and Deployment Mechanism

The parachute has a fabric that is super soft, light and tear-resistant quality. The parachute's design incorporates eight shock cords, which contribute to its structural integrity. These cords are engineered to possess both tensile strength and resistance to heat from the ejection charge.

- The drag equation mentioned before, rearranged to solve for d :
- $$d = \sqrt{\frac{8 \cdot m \cdot g}{\pi \cdot \rho \cdot V^2 \cdot C_d}} = \sqrt{\frac{8 \cdot 0.7 \cdot 9.81}{\pi \cdot 1.225 \cdot 4.5^2 \cdot 1.5}} = 0.77m$$



Figure 31: The parachute

The dimensional calculations were determined by the total mass and the desired descent rate. The shock cord, a synthetic material characterized by its elastic properties, was segmented into two sections: 60 centimetres from the body tube to the nose cone, and 6 centimetres from the swivel to the parachute itself as it can be seen in Figure 34. This configuration was selected to minimize stress on the attachment points.

The deployment of the parachute is contingent upon the utilization of a black powder ejection charge within the engines, which functions to disengage the rocket's nose cone from the body tube at apogee. This enables the parachute to be deployed. The system is initiated by the five-second delay inherent in the engines, a concept elaborated upon in Chapter 5. Prior to the integration of a swivel mechanism in the design, measures were implemented to avert the entanglement of the parachute chords during descent, thereby ensuring a seamless and regulated recovery.

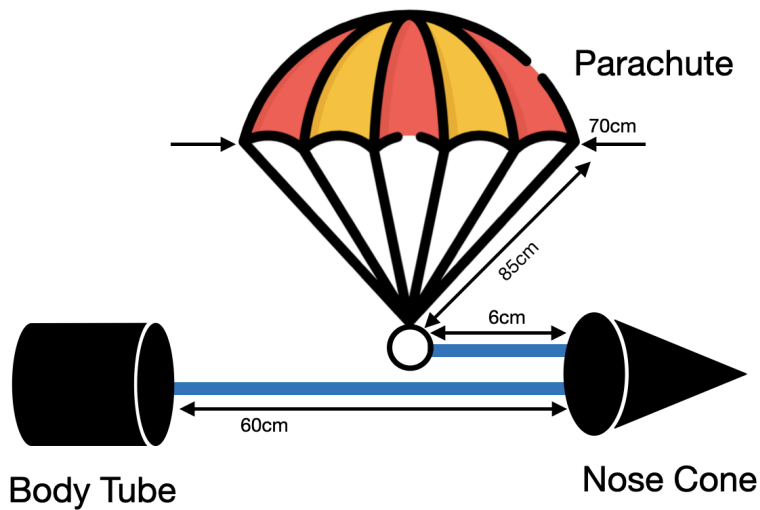


Figure 32: The parachute system with dimensions

8. Testing and Validation

As with all aerospace missions, there are some requirements that have to be set first and tests are designed to verify that each requirement is met. These requirements are about the rocket, the flight computer, the parachute and telemetry. Specifically, they ensure that the flight computer and sensors function correctly in the expected environment. The rocket structure is aerodynamically stable, the parachute recovery system deploys reliable and finally the telemetry systems stores flight data without significant are any losses.

| ID | Requirement Description | Verification Method |
|-----|--|-----------------------------------|
| R-1 | The flight computer shall collect sensor data (pressure, altitude, temperature, GPS, accelerometer, gyroscope, magnetometer) at a minimum rate of 1 Hz | Sensor data logging test |
| R-2 | The flight computer shall store data over a distance of at least 200 meters | Telemetry transmission range test |
| R-3 | The camera shall store video feed over a distance of at least 200 meters | Video Camera storing range test |
| R-4 | The parachute shall eject and deploy upon activation of the ejection system charges | Drop test and ejection test |
| R-5 | The power system shall operate for at least the entire mission duration (5 minutes) | Battery endurance test |
| R-6 | The GPS module shall acquire a fix and maintain position accuracy within ± 5 meters | GPS field test |
| R-7 | The aerodynamic stability margin shall be within ≥ 1.5 cal (calibers) to ensure a stable flight trajectory | Swing test |

Table 3: Requirement Description and Verification Method

8.1. Pre-Flight Electronics Validation

Starting with the sensor data, telemetry transmission and camera test (R-1, R-2, R-3) as they can be verified simultaneously. The objective is to verify that the sensors record accurate data and the Raspberry Pi shall store data and the camera stores video feed while it is at least over 200meters away from the ground station (which is the laptop). The procedure here is:

1. Power on the flight computer and connect it via ssh to a laptop.
2. Set up the Raspberry Pi for live data transmission and the camera.
3. Record sensor data and video feed while the system remains stationary.
4. Walk away from the ground station at increasing distances.
5. Complete the data collection and switch off the Raspberry Pi.
6. Check for data loss.

In order for the requirement to be successful the data should be recorded at $\geq 10Hz$ and that there is a stable transmission at 200meters with minimal to no data loss. On 20 March 2025, the test was successfully conducted by initially utilising live telemetry for the initial 60 metres, followed by the relocation of the flight computer after its disconnection from the Wi-Fi network and subsequent power interruption. Upon reconnection, it was determined that the flight computer continued to store data up at $1Hz$ to the point of the power interruption and the video feed was saved successfully.

8.2. Launch and Recovery Testing

In this test the objective is to ensure that the parachute eject and deploys successfully (R-3). The procedure would be:

1. Place the parachute and ejection system in the rocket.
2. Activate the parachute ejection charge.
3. Monitor the parachute deployment.

For the test to be successful, the parachute must deploy successfully. On 26 March 2025, the parachute was folded in accordance with the established protocol, prior to its deployment on the rocket. The parachute was then ejected by blowing air into the rocket, where the actual ejection charge will be located.

8.3. Battery Endurance Test

In this case the objective is the that the power system supports the mission duration without voltage drop (R-4). The procedure for this test is:

1. Fully charge the battery system.
2. Run the entire flight computer system, sensors, and transmission module for at least 5 minutes.
3. Monitor the battery over time to detect any disconnections.

For the test to be successful the voltage would have to remain stable and system operates continuously. On 21 March 2025, I first fully charged the battery, then run GPS test, which is the test for the GPS to connect to a satellite for 15 minutes and after that I ran the scripts that will also be used at the launch which are the data storing and video storing for another 10 minutes. Both tests were run 2 times more as the scheduled run time.

8.4. GPS Field Test

For the GPS field test (R-5) to be successful the objective is that the GPS maintains a reliable fix. The procedure here is:

1. Power on the flight computer and connect it via ssh to a laptop.
2. Record sensor data while the system remains stationary.
3. Move the system outdoors and verify that the GPS acquires a satellite fix.
4. Check logs for missing or incorrect data.

In order for the requirement to be successful the GPS shall have an accuracy within ± 5 meters.

8.5. Ground Testing of Aerodynamic stability Test

Continuing with the aerodynamic stability (R-6) the objective here is that the rocket's stability margin is ≥ 1.5 calibers. This would be tested with a swing test. The procedure is:

1. Find the rocket's CG.
2. Attach a string to the CG and spin it to check for stable flight behaviour.

As here it would be difficult to check the exact caliber number the pass criteria would be that the rocket maintains a stable flight path during the test.

8.6. Post-Flight Adjustments and Improvements

After the first flight that took place on

9. Results and Discussion

9.1. Overview of Test Flights

In total, there were 12 engines and as 3 engines are required per launch there were overall four launches to evaluate the rockets flight performance, to access the sensors reliability and finally to validate the accuracy of the simulation predictions in OpenRocket. The goal of each flight was to capture data such as temperature, barometric altitude, GPS altitude, velocity, vertical speed, acceleration magnitude, orientation (pitch, roll, yaw), rotation rate, and GPS path. All the sensors on the flight computer were thoroughly tested prior the launch as discussed in section 8. Finally on Table 4 you can see the conditions and weather data of each flight.

| Parameter | Flight 1 | Flight 2 | Flight 3 | Flight 4 |
|-----------------------|--------------|--------------|--------------|--------------|
| Launch Date | 25.03.2025 | 25.03.2025 | 25.03.2025 | 25.03.2025 |
| Launch Location | Thessaloniki | Thessaloniki | Thessaloniki | Thessaloniki |
| Launch Site Elevation | 100m | 100m | 100m | 100m |
| Temperature | 18°C | 18°C | 18°C | 18°C |
| Atmospheric Pressure | 1012hPa | 1012hPa | 1012hPa | 1012hPa |
| Relative Humidity | 45% | 45% | 45% | 45% |
| Wind Speed | 7.2km/h | 7.2km/h | 7.2km/h | 7.2km/h |
| Wind Direction | NW (320°) | NW (320°) | NW (320°) | NW (320°) |

Table 4: Flight Conditions and Environment Summary

9.2. Flight Data Analysis

This section presents the results of each flight, which were then compared with the simulation data.

9.2.1. Flight 1: Data overview

Flight 1 was conducted on the 30th of March 2025. As illustrated in Figure 33, the complete set of telemetry plots acquired from the inaugural flight is presented. The visualisation of these plots, which utilises a 1-Hz sampling rate, offers a comprehensive representation of the rocket's behaviour throughout all phases of its flight trajectory. The figure allows for the clear visualisation of the relevant data, blah blah blah. In the following section, a comparison is drawn between each plot and the simulations conducted using OpenRocket, with the incorporation of meteorological data to ensure the most precise results.

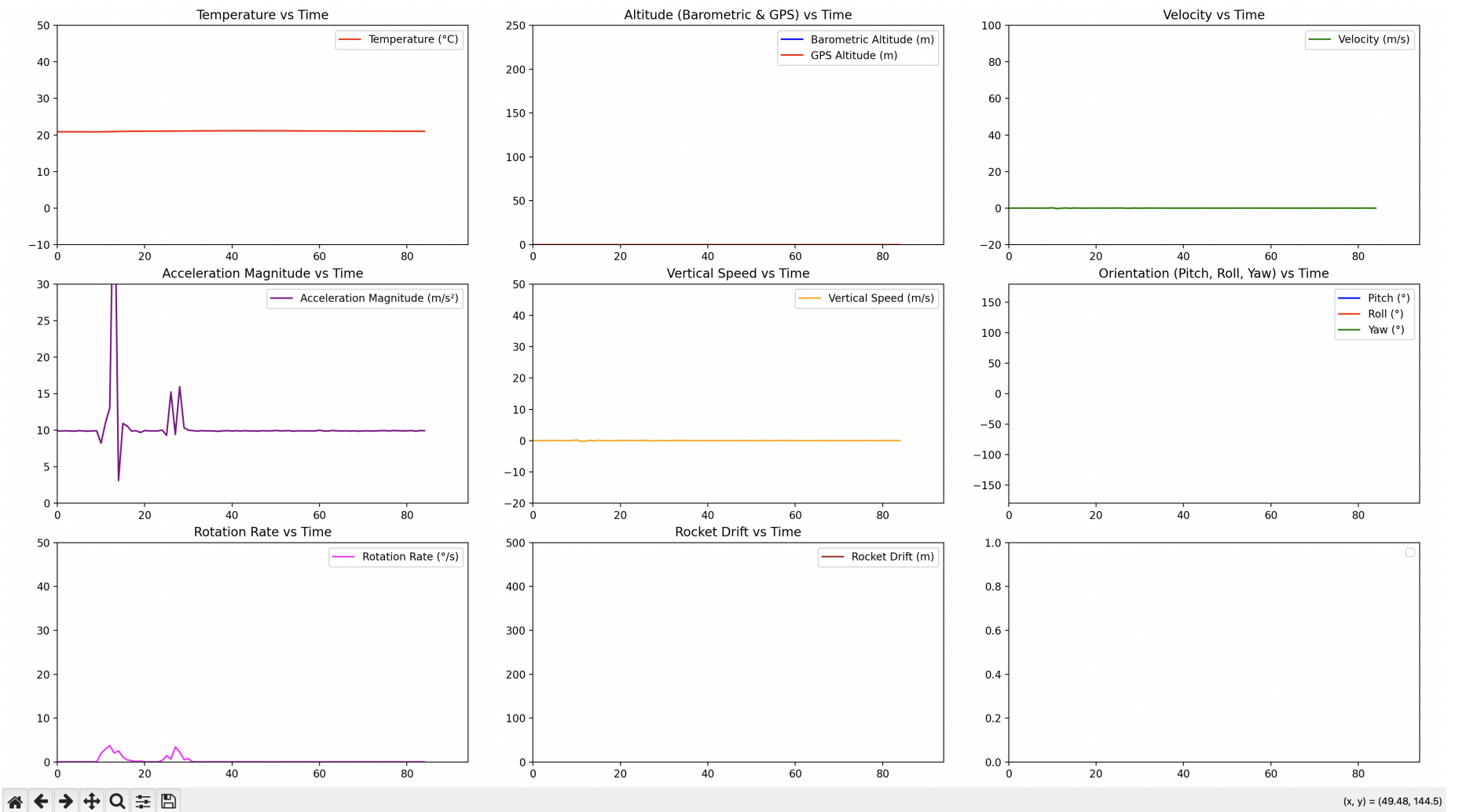


Figure 33: Telemetry data from the first flight

9.2.2. Flight 2: Data overview

1. Telemetry Plots
2. Camera Performance
3. Notes on anomalies or issues
4. Comparison with Open Rocket Simulation

9.2.3. Flight 3: Data overview

9.2.4. Flight 4: Data overview

9.3. Performance Comparison and Trends

1. Summary table of all four flights
2. Overlaid plots for comparison
3. Discuss how performance evolved and what factors contributed

9.4. Material and Structural Evaluation

1. Discuss PLA strength, durability after multiple flight any warping or cracking
2. Parachute deployment, fin attachment, and launch lug observations

9.5. Assessment of Flight Computer and Telemetry System

1. Reliability of sensors
2. Transmission range and telemetry clarity

10. Conclusion and Future Work

10.1. Summary of Findings

10.2. Limitations and Challenges Faced

10.3. Recommendations for Future Work

10.4. Potential Applications of the Hermes Rocket

References

- [Adafruit,] Adafruit. Adafruit industries, unique fun diy electronics and kits.
- [Apogee Components, 2023] Apogee Components, I. (2023). Peak of flight newsletter : Apogee rockets, model rocketry excitement starts here.
- [Barrowman and Boyce, 1966] Barrowman, R. and Boyce, D. (1966). Air distribution from lateral ducts in barley. Journal of Agricultural Engineering Research, 11:243–247.
- [Billington,] Billington, A. Optimizing strength of 3d printed parts.
- [Forum, 2017] Forum, Y. O. R. (2017). Ye olde rocket forum - national model and sport rocketry collection blog.
- [Hall, 2023] Hall, N. (2023). Four forces on a rocket | glenn research center | nasa.
- [MarkForged, 2024] MarkForged (2024). Pla vs abs vs nylon.
- [Niskanen, 2009] Niskanen, S. (2009). Development of an open source model rocket simulation software.
- [OpenRocket,] OpenRocket. Openrocket.
- [Printers,] Printers, P. D. Prusa 3d printers.
- [Sheetz, 2020] Sheetz, M. (2020). Inside relativity space's 3d-printing rocket 'factory of the future'.
- [Slump, 2021] Slump, G. (2021). Pla vs abs vs petg: The differences.
- [Stine and Stine, 2004] Stine, G. H. and Stine, B. (2004). Handbook of Model Rocketry. John Wiley Sons.
- [thrustcurve.org,] thrustcurve.org. Thrustcurve.
- [Wawryniuk et al., 2024] Wawryniuk, Z., Brancewicz-Steinmetz, E., and Sawicki, J. (2024). Revolutionizing transportation: an overview of 3d printing in aviation, automotive, and space industries. The International Journal of Advanced Manufacturing Technology.

A. CAD and 3D Print Files

B. Code Implementation

Descriptions and code details:

B.1. Raspberry Pi Sensor Reading Code

python

C. Component List and Costs

| SL | Component Name | Quantity | Price (\$) | Total (\$) |
|----|---|----------|---------------|---------------|
| 1 | Raspberry Pi Zero 2W | 1 | 16.74 | 16.74 |
| 2 | Raspberry Pi Hat | 1 | 9.61 | 9.61 |
| 3 | Adafruit DPS310 | 1 | 6.46 | 6.46 |
| 4 | Adafruit ICM-20948 | 1 | 13.90 | 13.90 |
| 5 | Adafruit Mini GPS PA1010D | 1 | 27.85 | 27.85 |
| 6 | Raspberry Pi Camera V3 Wide lens | 1 | 42.32 | 42.32 |
| 7 | 3A USB step-down voltage regulator module DC-DC Converter | 1 | 0.88 | 0.88 |
| 8 | LP903450 3.7V 1600mAh Lithium Polymer Battery | 2 | 14.00 | 28.00 |
| 9 | Charger for Battery | 1 | 3.70 | 3.70 |
| 10 | STENNA QT/Qwiic cable | 3 | 0.884 | 2.652 |
| 11 | Raspberry Pi Zero Camera Cable | 2 | 2.43 | 4.86 |
| 12 | Spectrum PETG Filament | 1 | 21.90 | 21.90 |
| 13 | Sandpaper | 3 | 0.60 | 1.80 |
| 14 | JB-WELD Plasticbonder | 2 | 8.50 | 17 |
| 15 | Klima D9-5 Engines (pck 6) | 2 | 33.25 | 66.50 |
| 16 | TOTAL | 20 | | 264.172 |

Table 5: Component List and Costs